JGR Oceans

RESEARCH ARTICLE
10.1029/2020JC017097

High-Resolution Numerical Modeling of Barotropic Global Ocean Tides for Satellite Gravimetry

R. Sulzbach[1,2], H. Dobslaw[1], and M. Thomas[1,2]

[1]Deutsches Geoforschungszentrum (GFZ), Potsdam, Germany, [2]Institut für Meteorologie, Freie Universität Berlin (FUB), Berlin, Germany

Key Points:

- A new barotropic tidal model with rotated numerical pole and full self-attraction and loading potential is introduced
- The solution accuracy is nearly constant over a wide range of frequencies and only weakly dependent on the potential amplitude
- Two partial tide solutions exhibit a smaller deviation from tide gauge data than solutions built on altimetric data and admittance assumptions

Supporting Information:

Supporting Information may be found in the online version of this article.

Correspondence to:

R. Sulzbach,
sulzbach@gfz-potsdam.de

Citation:

Sulzbach, R., Dobslaw, H., & Thomas, M. (2021). High-resolution numerical modeling of barotropic global ocean tides for satellite gravimetry. *Journal of Geophysical Research: Oceans*, *126*, e2020JC017097. https://doi.org/10.1029/2020JC017097

Received 18 DEC 2020
Accepted 7 MAY 2021

Abstract The recently upgraded barotropic tidal model TiME is employed to study the influence of fundamental tidal processes, the chosen model resolution, and the bathymetric map on the achievable model accuracy, exemplary for the M_2 tide. Additionally, the newly introduced pole-rotation scheme allows to estimate the model's inherent precision (open ocean rms: 0.90 cm) and enables studies of the Arctic domain without numerical deviations originating from pole cap handling. We find that the smallest open ocean rms with respect to the FES14-atlas (3.39 cm) is obtained when tidal dissipation is carried out to similar parts by quadratic bottom friction, wave drag, and parametrized eddy-viscosity. This setting proves versatile to obtaining high accuracy values for a diverse ensemble of additional partial tides. Using the preferred model settings, we show that for certain minor tides it is possible to obtain solutions that are more accurate than results derived with admittance assumptions from data-constrained tidal atlases. As linear admittance derived minor tides are routinely used for de-aliasing of satellite gravimetric data, this opens the potential for improving gravity field products by employing the solutions from TiME.

Plain Language Summary We introduce the upgraded computer model TiME, that simulates ocean tides originating from the gravitational attraction of the sun and moon. The model relies on the physics of relevant processes without incorporating actual observations of water level variations. Formerly unconsidered effects that strongly impact tidal dynamics are now included. We discuss the individual impact of these effects on the model accuracy, which is estimated relatively to local measurements from tide gauges. We further compare our results to external tidal models, that employ satellite observations for increased accuracy. Here we find that the upgraded model performs well in the open ocean, and has a reduced accuracy in shallow and coastal waters. The final model setting can simulate tides that recur once or twice per day at a similar level of accuracy. This weak dependence on the excitation amplitude renders TiME especially suited for studying minor tides. Due to their low amplitudes, these tides make up a smaller part of tidal dynamics and are hard to determine with satellite data, thus rendering solutions by our model being free of data constraints valuable. Comparing our solutions with routinely used, empirically motivated estimates of minor tides we show that an increased accuracy is obtained.

1. Introduction

Signatures of ocean tidal dynamics are omnipresent in oceanographic and geodetic observations taken either on the ground or from space. This includes periodic variations in ocean currents registered by moored instruments or acoustic tomography (Dushaw et al., 1997; Luyten & Stommel, 1991; Ray, 2001) as well as by induced secondary magnetic fields (Maus & Kuvshinov, 2004; Saynisch et al., 2018), sea surface height changes measured from tide gauges and satellite altimetry (Doodson, 1928; Schrama & Ray, 1994), and global bottom pressure variations from pelagic pressure recorders and gravimetric satellite missions (Wiese et al., 2016). More recently, even tiny variations in sea surface temperature (Hsu et al., 2020) and tropical precipitation observations (Kohyama & Wallace, 2016) were related to ocean tidal dynamics.

Separating tidal and transient signals in satellite records is not trivial due to the complicated spatio-temporal sampling of observations taken from satellites in non-geostationary orbits. The repeat orbit of the TOPEX/Poseidon (T/P) satellite altimetry mission (Fu & Cazenave, 2000) has been carefully selected in a way that aliases the major ocean tidal constituents into periods that are well distinct from naturally occurring periodicities, thereby providing tidal charts based on observations that cover the open ocean in a regular spatial pattern (Shum et al., 1997). After assimilating tidal elevations from T/P

and other altimetry missions into hydrodynamic models (Carrere et al., 2015; Egbert & Erofeeva, 2002; Taguchi et al., 2014) or using these data to construct empirical corrections to an adopted model (Cheng & Andersen, 2011; Fok, 2012; Ray, 1999; Savcenko et al., 2012), those models are extensively used for the processing of unrelated observations, as e.g., satellite gravimetry missions. Presently, all 34 tidal constituents given by the FES14 tidal atlas (Carrere et al., 2015; Lyard et al., 2006) are directly removed from Gravity Recovery And Climate Experiment (GRACE) and GRACE Follow-on (GRACE-FO) data, and more than 300 additional minor constituents inferred by admittance methods are also subtracted (Kvas et al., 2019). The existing weaknesses in present-day admittance methods, however, have been discussed extensively in the past (Ray, 2017), so that explicit tidal simulations with unconstrained numerical ocean tide models provide potentially valuable information on tidal lines less well constrained by satellite altimetry.

The sensitivity of satellite gravimetry to periodic mass re-distributions in the Earth system is expected to increase even further when the full potential of the satellite-to-satellite tracking by means of laser ranging interferometry (Ghobadi-Far et al., 2020) is also used for gravity field processing. Employing end-to-end satellite simulations, Flechtner et al. (2016) found that ocean tide errors are among the top three factors that limit the accuracy of global mass distribution estimates from GRACE-FO. Various concepts of multi-satellite constellations are currently being evaluated by space agencies in Europe, the US, and China for possible implementation as a next-generation gravity mission (e.g., Hauk and Wiese [2020]). Scientific requirements and user demands for such new missions almost always request higher spatial resolution and greater accuracy (see Pail et al., 2015). Equivalently, in order to re-process the already existing data record from GRACE and GRACE-FO into more precise time-series of terrestrial water storage and ocean bottom pressure suited for climate monitoring (Tapley et al., 2019), better ocean tide models are critically important.

While data-constrained tidal models provide highly accurate estimates of tidal constituents in regions where altimetry data is dense (open ocean residuals below 1 cm), model accuracy decreases as the data quality decreases (minor tides, polar, and shelf areas). In effect, the ratio of model uncertainty to signal typically increases considerably for tidal excitations with smaller amplitudes (Stammer et al., 2014). Even more, additional errors can be introduced, when estimating minor tidal excitations with admittance methods. These deviations might be reduced by the explicit numerical modeling of minor tides.

In this contribution, we present efforts toward extending a hydrodynamic model of ocean tidal dynamics particularly suited to study minor and compound tides. Our work is based on the Tidal Model forced by Ephemerides (TiME; Weis et al., 2008) introduced in Section 2. We describe various improvements to the numerics of the model including the rotation of the poles (Section 3), an extension of the physical model by implementing explicitly the effects of self-attraction and loading (Section 4) and the incorporation of topographic wave drag as a new dissipation mechanism (Section 5). Exemplary for the principal semidiurnal lunar tide M_2, we will report about the accuracy of the simulated tidal heights both with respect to tide gauge data and the state-of-the-art global tide solution FES14 that is constrained by observations. Various sensitivity experiments are presented documenting the individual contributions of the various changes made to TiME in terms of achieved accuracy (Section 6). The paper is augmented with an assessment of energy dissipation patterns of the model and additional simulations of partial tides in the diurnal and semidiurnal tidal bands (Section 7). Building on the results of previous chapters, we focus in Section 8 on selected minor tides that can be simulated with higher accuracy than solutions constructed from linear admittance estimates on data-constrained models. Finally, the article is closed with a summary (Section 9).

2. Tidal Model Forced by Ephemerides (TiME)

The barotropic ocean model presented in this contribution is based on decade-long work to simulate global ocean tides in Hamburg, Germany. Starting from the fundamental work of Wilfried Zahel (Zahel, 1977, 1978), unconstrained hydrodynamic models were used to quantify the contributions of ocean tides to Earth rotation (Seiler, 1991), the evolution of tides since the last glacial maximum, and its consequences for oceanic torques acting on the solid Earth (Thomas & Sündermann, 1999), interactions among

ocean tides and the general circulation (Thomas et al., 2001), and the identification of free barotropic normal modes in the world's ocean under the influence of friction and sea-bottom deformations caused by surface loading (Zahel & Müller, 2005).

We start our work with the Tidal Model forced by Ephemerides (TiME) as described by Weis et al. (2008), which simulates global barotropic tidal dynamics by solving the nonlinear shallow water equations (e.g., Pekeris, 1974)

$$\partial_t \mathbf{v} + \mathbf{f} \times \mathbf{v} + \left(\mathbf{v} \cdot \nabla\right)\mathbf{v} \quad = \quad -g\nabla\left(\zeta - \zeta_{SAL} - \zeta_{eq}\right) - \frac{r}{H} \mid \mathbf{v} \mid \mathbf{v} + \hat{\mathbf{R}}\mathbf{v} \tag{1}$$

$$\partial_t \zeta \quad = \quad -\nabla\left((H + \zeta)\,\mathbf{v}\right) \tag{2}$$

determining $\boldsymbol{\zeta}(\phi,\lambda,t) = (\mathbf{v},\zeta) \in \mathbb{R}^3$, with sea surface elevation ζ tidal flow velocity $\mathbf{v}$, latitude ϕ and longitude λ. Here, $\mathbf{f} = 2\Omega \sin\phi\ \mathbf{e_{vert}}$ is the Coriolis vector, $\Omega = \frac{2\pi}{1\mathrm{d}}$ (d = 1 sidereal day) and $g = 9.80665\frac{m}{s^2}$ is the surface gravity, H describes the depth from undisturbed surface to sea-bottom, r denotes the quadratic bottom friction coefficient and

$$\hat{\mathbf{R}}\mathbf{v} = \frac{A_h}{R_{earth}^2}\left(\frac{\partial_\lambda^2}{\cos\phi} + \partial_\phi^2 - \tan\phi\,\partial_\phi - (1 + \tan^2\phi)\right)\begin{pmatrix} u \\ v \end{pmatrix} - \frac{A_h}{R_{earth}^2}\left(2\tan\phi\,\partial_\lambda\right)\begin{pmatrix} v \\ u \end{pmatrix} \tag{3}$$

parametrizes horizontal turbulence as eddy viscosity. Here the horizontal eddy-viscosity coefficient A_h and the earth-radius $R_{\mathrm{earth}} = 6{,}371$ km were introduced. The principal forcing term $g\nabla\,\zeta_{eq} = \nabla V_{tid}$ can either be an individual partial tide excitation or the full luni-solar tidal potential as quantified by the ephemeridies of sun and moon (Bartels, 1957). Since TiME considers nonlinear accelerations arising mainly from bottom-friction ($-r/H|\mathbf{v}|\mathbf{v}$), advection ($-(\mathbf{v}\cdot\nabla)\mathbf{v}$) and the wave-drift-term ($-\nabla\cdot(\zeta\mathbf{v})$), full ephemeridic forcing enables interactions between individual partial tides (compare also Einšpigel and Martinec [2017]). Time-variable surface loading from ocean tidal elevations causes elastic deformation of the sea-bottom that induces a secondary gravity potential (Hendershott, 1972). Weis et al. (2008) approximated the effect as a fraction ϵ of the local tidal elevation, setting $\zeta_{SAL} = \epsilon\zeta$ as introduced before by Accad and Pekeris (1978). Typical values for ϵ are between 0.08 and 0.12.

When considering forcing by a single tidal constituent of frequency ω, the tidal solution converges to

$$\zeta(\mathbf{x},t) = \Re\left(\sum_{n=0}\zeta^{n\omega}(\mathbf{x})\,e^{in\omega t}\right) \tag{4}$$

$$= \zeta_{cos}^{\omega}\cos\omega t + \zeta_{sin}^{\omega}\sin\omega t + \left(\zeta_{const}^{\omega} + \zeta_{cos}^{2\omega}\cos 2\omega t + \zeta_{sin}^{2\omega}\sin 2\omega t + \ldots\right), \tag{5}$$

where $\boldsymbol{\zeta}^{n\omega}(\mathbf{x}) \in \mathbb{C}^3$ describes the part of the field oscillating at frequency $n\omega$, comprised of *in-phase* $\zeta_{cos}^{n\omega}$ and *quadrature* component $\zeta_{sin}^{n\omega}$. The vast majority of tidal dynamics is hereby described by the part of the field oscillating at frequency ω. The residual tidal circulation ζ_{const}^{ω}, consequence of tidal rectification (e.g., Pérenne & Pichon, 1999), as well as the overtides with $n \geq 2$ are the result of said nonlinear interaction, representing minor contributions to the tidal flow field. Equations 1 and 2 are solved on a global, regular latitude-longitude grid at a resolution of $\frac{1^\circ}{12}$ employing a semi-implicit finite-difference algorithm as described in Backhaus (1983) and Backhaus (1985). Since the smallest zonal grid-cell size limits the time-step, the zonal resolution is reduced at two certain latitude circles toward the North Pole and finalized by a spherical cap to avoid a polar coordinate singularity. Numerical experiments were based on global Gebco (GEBCO Compilation Group, 2019) and Etopo1 (NOAA, 1988) bathymetries, where the best results presented in Weis et al. (2008) were obtained with Gebco data. Results from this model configuration will be presented in Section 6 in comparison to the latest results that incorporate various extensions to the model physics as outlined in the following.

Figure 1. Selected numerical grids used for experiments with TiME, defined by the position of their numerical North Pole on a standard lat-lon grid. The poles of grid (a), labeled (Aus), are positioned in Australia (dry pole) and the North Atlantic (wet pole) at $\phi, \lambda = (24°\text{N}, 45°\text{W})$. Grid (b), having its poles in Greenland/Antarctica (Gre) at (75°N, 40°W) and grid (c), with poles in China/Argentina (Chi) at (28.5°N, 114.5°E) do not have wet numerical poles and thus do not require a pole cap.

3. Pole Rotation Scheme and Tide-Raising Potential

Positioning a pole of the numerical grid in the middle of the Arctic ocean requires the application of a spherical cap in order to work around the singularity. This can be avoided by shifting the pole locations to dry grid cells that are ignored by the solver. In order to adapt the numerical scheme to the rotated pole location, we transform the explicitly space-dependent parts of the shallow water Equations 1 and 2, comprising bathymetric function $H(\phi, \lambda)$, tide-raising potential $V_{tid} = g\zeta_{eq}(\phi, \lambda)$ and Coriolis vector $\mathbf{f}(\phi, \lambda)$ into a new coordinate system which is spanned by the rotated coordinates $\phi'(\phi, \lambda)$, $\lambda'(\phi, \lambda)$. This coordinate transformation

$$\sin\phi = \cos\phi' \cos\phi_p \cos(\lambda') + \sin\phi_p \sin\phi' \tag{6}$$

$$\tan(\lambda - \lambda_p) = \frac{\sin(\lambda')}{\sin\phi_p \cos(\lambda') - \cos\phi_p \tan\phi'}, \tag{7}$$

where ϕ_p, λ_p is the location of the new North Pole on the unrotated grid, can immediately be used to transform the Coriolis factor $f(\phi) = f\sin(\phi)$. Due to the different local definitions of north and east on a rotated grid, special attention has to be spent when transforming vectorial quantities (e.g., the tidal velocity field $\mathbf{v}$).

In total, 4 different pole locations (see Figure 1) are implemented for experiments: The original latitude-longitude grid with the pole in the Arctic at 90° N (following denoted Arc), and two realizations with land-covered poles at Argentina and China (Chi) and Antarctica and Greenland (Gre), with dry areas around the poles having a radius of at least 4°. An additional configuration with the South Pole in Australia and the North Pole in the North Atlantic (Aus) was also implemented to highlight the potential errors that might be introduced from a poorly selected grid configuration. In the following, the consequences of the pole rotation scheme for bathymetry and tide-raising potential are discussed.

Previously, TiME was run with Gebco and Etopo1 bathymetries. More recently, the high-resolution Rtopo2 data (Schaffer et al., 2016) became also available. Based on Gebco data, the Rtopo2 grid uses additional data sources in polar latitudes with a special focus on accurately representing sub-ice-shelf cavities as the position of the ice-shelf grounding line is known to have a strong effect on tidal oscillations (Arbic, Karsten, & Garrett, 2009; Wilmes & Green, 2014). We included these areas by considering the water-column height as the difference between the ice base and bedrock depth. Since the resolution of our tidal model (5 arc minutes) is well below the resolution of the available bathymetric data (30 arc seconds), special attention has been paid to how the necessary resolution reduction is optimally performed. We employ an interpolation strategy motivated by perturbation theory, that uses conservative interpolation of inverse depth (1/H), to directly derive bathymetric maps for the respective pole-orientations (Arc/Chi/Gre/Aus) from high-resolution data (see supporting information). The minimum water depth was set to 15 m as by Weis et al. (2008), while values of 10 or even 5 m have a negligibly small influence on tidal dynamics. The Caspian Sea Level (CSL) that is subject to climatic rapid changes compared to the open ocean (Chen et al., 2017; Naderi Beni et al., 2013) has been fixed to −26.5 m.

The luni-solar tide-raising potential acting on the oceans at epoch t

Table 1
Love Number Used in TiME Taken From Spiridonov (2018) for the Diurnal Partial Tide Spectrum (Degree 2) and for Semidiurnal and Terdiurnal Partial Tides of Degree l = 2 (d2) and Degree l = 3 (d3)

Tide	σQ_1	Q_1	$\rho 1$	O_1	P_1	K_1	$\Psi 1$	$\phi 1$	OO1	d2	d3
h_l^b	0.602	0.601	0.601	0.600	0.578	0.519	1.079	0.666	0.606	0.606	0.290
k_l^b	0.296	0.296	0.296	0.296	0.284	0.255	0.536	0.329	0.299	0.299	0.091
a_l^b	0.694	0.695	0.695	0.696	0.706	**0.736**	**0.457**	0.663	0.693	0.693	**0.801**

Note. Coupling to Earth's NDFW-resonance renders Love numbers in the diurnal band dispersive. Strong deviations from d2 are plotted **bold**.

$$V_{tid}(\phi,\lambda,t) = \sum_{l=2}^{l}\sum_{m=0}^{l}\bar{P}_{lm}(\cos\phi)\sum_i a_l^b(\omega_i)\left(c_i^{lm}\cos(m\lambda+\omega_i t)+s_i^{lm}\sin(m\lambda+\omega_i t)\right) \tag{8}$$

can be decomposed into orthonormal, real-valued spherical harmonics Y_{lm} with time-dependent coefficients. These coefficients can further be decomposed into temporally harmonic constituents at discrete frequencies ω_i with amplitudes s_i^{lm}, c_i^{lm} (Hartmann & Wenzel, 1995). Here $\bar{P}_{lm}$ are orthonormal Legendre-Functions (e.g., Heiskanen & Moritz, 1967) and $a_l^b(\omega_i) = 1 + k_l^b(\omega_i) - h_l^b(\omega_i)$ is a combination of Love numbers (Love, 1909) that encrypts the action of (elastic) body tides of the solid Earth on oceanic tides. The frequency dependence of $a_l^b(\omega_i)$ originates from a coupling of tidal motions to the near diurnal free wobble (NDFW), one of the fundamental eigenmodes of the solid Earth (Wahr, 1981; Wahr & Sasao, 1980), which has prominent effects on admittances in the K_1 tidal group (Ray, 2017).

We use the tidal catalog published by Hartmann and Wenzel (1995) considering contributions up to degree $l = 3$, so that minor ocean tides even of third degree origin (e.g., M_3) can be simulated. $a_l^b(\omega_i)$ up to degree-3 has been taken from Spiridonov (2018) (model 9), where diurnal Love numbers are calculated by linear interpolation from neighboring data-points (linear Admittance, see Table 1). Please note that due to the frequency-dispersion and degree dependence introduced by $a_l^b(\omega_i)$, the ocean tide-raising potential differs from the initial gravitational potential created solely by sun and moon.

Since V_{tid} is composed of few low-degree spherical harmonics, transformation to rotated-pole grids can be performed efficiently by utilizing Wigner-D-functions initially derived in the framework of quantum theory of angular momentum (e.g., Warschalowitsch et al., 1988). Dependent on ϕ_p and λ_p a single component c_i^{lm}/s_i^{lm} of $V_{tid}(\phi, \lambda, t)$ transforms into a combination of spherical harmonics of the same degree. The rotation is therefore entirely described by a transformation $\hat{T}(\phi_p,\lambda_p)$ of coefficients c_i^{lm}/s_i^{lm} to the new set of coefficients $\tilde{c}_i^{lm}/\tilde{s}_i^{lm}$ valid in the rotated frame, reading

$$\hat{T}(\phi_p,\lambda_p)\cdot\begin{pmatrix}c_i^{lm} & s_i^{lm}\end{pmatrix} = \begin{pmatrix}\tilde{c}_i^{lm} & \tilde{s}_i^{lm}\end{pmatrix}. \tag{9}$$

Here $(c_i^{lm} \quad s_i^{lm})$ describes a set of $2l + 1$ coefficients of the same degree. This transformation is implemented by using the rotation algorithm by Gooding and Wagner (2010) following routines published by Risbo (1996).

The maximum dry radius around the North and the South Pole of 4° defines the smallest zonal resolution on this equally distributed lat-lon grid. Since this distance restricts the minimum possible time-step, it was necessary to introduce additional zones of reduced zonal resolution to the Southern Hemisphere. In Weis et al. (2008), this was solely implemented for the Northern Hemisphere since former bathymetries provided a much bigger dry radius around the South Pole (compare Figure 5). This modification allows the enlargement of the time-step by the factor of 4 and thus provides a considerable speed up. For all experiments shown in this paper, zonal resolution is first halved at $\phi = \pm 60°$ and afterward at $\phi = \pm 75°$ ensuring that zonal resolution varies between the margins of $\frac{1°}{12}$ and $4\sin(4°)\frac{1°}{12} \approx \frac{1°}{43}$ on the **gre**-grid ($\frac{1°}{38}$ on **chi**). The

model time-step was set to $\frac{1}{240}\left(\frac{1}{480}\right)$ of the respective tidal period for semidiurnal (diurnal) tides, yielding numerical values close to 180 s. All subsequent simulations have been initialized for at least 60 (30) complete periods for semidiurnal (diurnal) tides before harmonic constituents are estimated.

4. Self Attraction and Loading

The elastic deformation of the sea-bottom in response to a water load induces a secondary gravity potential that itself excites a response in ocean dynamics. The inclusion of this so-called self attraction and loading (SAL) potential $V_{\mathrm{SAL}} = g\zeta_{\mathrm{SAL}}$ has been found to be important many years ago (Hendershott, 1972). Since the additional local forcing depends on the entire global distribution of tidal elevations, it can be computed by a convolution integral. Such computations are rather costly, so that local parametrization of SAL (e.g., Accad & Pekeris, 1978) were often applied. However, present-day accuracy demands on global ocean tide models make a rigorous consideration of SAL indispensable (Ray, 1998). We consider SAL in the spectral domain, where the computation translates to a set of algebraic operations on spherical harmonic coefficients ζ_{nm}, reading

$$\zeta_{SAL}(\mathbf{x}) = \sum_{l,|m|\leq l} \frac{3\rho_{sw}}{\rho_{se}} \frac{\alpha_l}{2l+1} \zeta_{lm} Y_{lm}(\mathbf{x}), \tag{10}$$

where $\zeta(\mathbf{x}) = \sum_{l,|m|\leq l}\zeta_{lm}Y_{lm}(\mathbf{x})$, $\rho_{sw} = 1024\frac{kg}{m^3}$ and $\rho_{se} = 5510\frac{kg}{m^3}$ being the mean density of sea water and solid Earth, respectively.

Here, $\alpha_l = 1 + k_l - h_l$ is a combination of degree dependent Load-Love numbers (LLNs) (Munk & MacDonald, 1960) that encode the effects of additional gravitation (1), as well as seafloor deformation (h_l) and potential shift (k_l) caused by the varying water mass. The factor $\alpha_l/(2l+1)$ decreases with rising degree l, within ensuring slow but steady convergence, thus avoiding Gibbs Phenomenon at coastal load discontinuities (Agnew, 2007; Hewitt & Hewitt, 1979). We employ LLNs of Wang et al. (2012) (PREM Earth model) with a correction to represent low degree LLNs in the frame of figure (Blewitt, 2003). Further we set l_{max}, the maximum considered degree in Equation 10, to 1024, thereby guaranteeing sub-mm accuracy in SAL-representation apart from some shelf areas and estuaries as also incorporated and discussed before by Schindelegger et al. (2018). The computational burden is thereby shifted to repeated transformations between the spectral and the spatial domain, which are efficiently handled with the highly optimized SHTNS-package by (Schaeffer, 2013).

5. Topographic Wave Drag

A realistic representation of dissipative forces is critically important for modeling the system's resonant coupling to oceanic normal modes and has been the main issue in numerical tidal modeling for a long time. Besides turbulent friction of the bottom boundary-layer, which is strongest in shallow water, the inversion of satellite altimetry data indicated that significant dissipation is happening in the deep ocean located at prominent topographic features (Egbert & Ray, 2000, 2001). The reason for this energy loss from barotropic tides is the excitation of baroclinic tidal motion, known as internal tides (e.g., St. Laurent et al., 2012; Wunsch, 1975). This phenomenon is hard to observe with remote sensing techniques since the induced changes in the ocean state are nearly entirely internal. However, it was possible to detect the minuscule ocean surface fingerprint of internal tides with space-geodetic techniques (e.g., Zhao, Alford, Girton, Johnston, & Carter, 2011; Zhao, Alford, Girton, Rainville, & Simmons, 2016). Further dissipation is expected from shallow water processes, horizontal turbulent friction and friction at ice-water boundaries in polar latitudes.

The explicit simulation of internal tides requires a depth-resolving, baroclinic ocean general circulation model (Arbic et al., 2012) and is hence much more complex than barotropic tidal modeling as pursued here. Nonetheless, parametrizations for baroclinic processes are available from theoretical considerations and have shown to be able to capture the dissipation patterns accurately (Buijsman et al., 2015; Green &

Nycander, 2013). We implement a parametrization proposed by (Nycander, 2005) that builds on previous considerations of Bell (1975) and Llewellyn Smith and Young (2003). It is based on linear wave theory and produces dissipation patterns that closely match available observations. The wave drag information is described by the second rank tensor $\mathbb{C}$. The drag then enters the tidal partial differential equation (PDE) as an additional dampening acceleration

$$\mathbf{a}_{\mathbf{iw}} = -\frac{1}{H}\mathbb{C}\cdot\mathbf{v}\,. \tag{11}$$

We use depth-resolved hydrographic data from the World Ocean Database for salinity (Zweng et al., 2018) and temperature (Locarnini et al., 2019) with the TEOS-10 equation of state (McDougall & Barker, 2011) to compute a global map of the buoyancy-frequency $N(\phi, \lambda, z)$, where z is a depth coordinate. The excitation of internal waves is a strongly frequency-dependent process that differs for diurnal ($\omega_d = \Omega$), semidiurnal $\left(\omega_{sd} = \frac{\Omega}{2}\right)$ and terdiurnal $\left(\omega_{td} = \frac{\Omega}{3}\right)$ tidal species resulting in different wave drag tensors for each species ($\mathbb{C}_{d/sd/td}$). As Buijsman et al. (2015), we follow the approach introduced and developed by Nikurashin and Ferrari (2011), Melet et al. (2013), and Scott et al. (2011) to reduce potentially overestimated wave drag-strength at supercritical slopes. To achieve this, the drag strength is normalized at supercritical slopes by its criticality squared to compensate for overestimated dissipation. Further, we allow for a tuning parameter κ to adjust the overall dissipation strength and introduce a cutoff depth of 150 m below which shelf oceans are assumed to be well-mixed. For more detail about calculation and properties of $\mathbb{C}$ consider the supporting information.

With the discussed wave drag-parametrization, TiME now includes three dominant dissipation mechanisms comprised in the dissipation operator $\mathbb{D}$. This further encompasses parameterized turbulent horizontal eddy-viscosity $\hat{\mathbf{R}}$ (Zahel, 1977) and quadratic bottom friction. Alltogether, Equation 1 can be rewritten as

$$\begin{aligned} \partial_t\mathbf{v} + \mathbf{f}\times\mathbf{v} + \left(\mathbf{v}\cdot\nabla\right)\mathbf{v} &= -g\nabla\left(\zeta - \zeta_{SAL} - \zeta_{eq}\right) - \mathbb{D}\,, \\ \text{with}\quad \mathbb{D} &= \frac{r}{H}\left|\mathbf{v}\right|\mathbf{v} - \hat{\mathbf{R}}\mathbf{v} + \frac{\kappa}{H}\mathbb{C}\mathbf{v}\,. \end{aligned} \tag{12}$$

By tuning the parameters κ, A_h and r model dissipation channels can be weighted individually.

6. Tidal Elevations for M_2 from TiME

In order to highlight the importance of individual model changes to TiME as given in the previous sections, we now report results from a number of sensitivity experiments for the principal lunar tide M_2 as outlined in Table 2. The model performance will be benchmarked against a data set comprised of 151 tide gauge stations compiled by Ray (2013) as well as the global state-of-the-art tidal atlas FES2014 (Carrere et al., 2015; Lyard et al., 2006), that was produced by Noveltis, Legos and CLS and distributed by Aviso +, with support from CNES(https://www.aviso.altimetry.fr/). Misfits will be reported in terms of time averaged rms

$$\mathrm{rms}_{\zeta_1^\omega,\zeta_2^\omega}(\mathbf{x}) = \sqrt{\frac{1}{T}\int_0^T dt\left(\mathrm{Re}\left(\zeta_1^\omega(\mathbf{x},t) - \zeta_2^\omega(\mathbf{x},t)\right)\right)^2} = \sqrt{\frac{1}{2}\left|\zeta_1^\omega(\mathbf{x}) - \zeta_2^\omega(\mathbf{x})\right|^2}\,, \tag{13}$$

that can be further averaged over a certain ocean domain D_o with area A_o yielding the space-averaged $\overline{\mathrm{rms}}_{\zeta_1^\omega,\zeta_2^\omega} = \sqrt{A_o^{-1}\sum_{\boldsymbol{x}_{ij}\in D_o} A_{ij}\left(rms_{\zeta_1^\omega,\zeta_2^\omega}(\boldsymbol{x}_{ij})\right)^2}$. We calculate averages for shallow water if the ocean depth is smaller than $H = 1{,}000$ m (10.4% ocean surface) or open ocean if the depth exceeds this limit (83.0% ocean surface). Both areas are restricted to latitudes with $|\phi| < 66°$ as altimetry data in these region is dense and guarantees a high quality of derived tidal atlases. When mentioned in the following sections, the results for $\overline{rms} = (a,b)$ are relating to validations with FES2014 (a) and pelagic tide gauges (b), where TG-results for Equation 13 are quadratically averaged over all stations.

Table 2
Open Ocean $\overline{rms}$ and Tidal Dissipation for an Ensemble of M_2 Tidal Simulations

ID	Grid	Pole	Bath.	SAL	$\varkappa$[%]	$A_h\left[\frac{m^2}{s}\right]$	$\overline{rms}$[a] [cm]	Dissipation[b] [TW]
RE	1°/12°	Chi	Rtopo2	d/o = 1024	125	2×10^4	3.39/4.83	2.70 (0.90/0.91/0.88)
P1	1°/12°	Arc	Rtopo2	d/o = 1024	125	2×10^4	4.08/5.19	2.61 (0.88/0.82/0.91)
P2	1°/12°	Gre	Rtopo2	d/o = 1024	125	2×10^4	3.6/5.21	2.76 (0.95/0.87/0.94)
P2b	1°/12°	Gre	Rtopo2	d/o = 1024	160	1.6×10^4	3.63/5.00	2.69 (0.88/1.00/0.78)
P3	1°/12°	Aus	Rtopo2	d/o = 1024	125	2×10^4	4.75/5.57	2.59 (0.70/1.01/0.82)[c]
B1	1°/12°	Chi	Gebco[d]	d/o = 1024	125	2×10^4	6.49/7.35	2.84 (0.95/0.94/0.95)
B2	1°/12°	Chi	Etopo1[d]	d/o = 1024	125	2×10^4	7.86/9.75	3.06 (1.07/1.03/0.97)
S1	1°/12°	Chi	Rtopo2	d/o = 100	125	2×10^4	3.38/4.82	2.69 (0.90/0.91/0.89)
S2	1°/12°	Chi	Rtopo2	d/o = 10	125	2×10^4	3.99/5.63	2.69 (0.90/0.90/0.89)
S3	1°/12°	Chi	Rtopo2	$\epsilon = 0.1$	125	2×10^4	5.41/6.69	2.94 (0.96/1.03/0.95)
S4	1°/12°	Chi	Rtopo2	None	125	2×10^4	22.91/27.02	3.30 (1.22/1.09/0.99)
W0	1°/12°	Chi	Rtopo2	d/o = 1024	150	5×10^2	4.03/6.54	2.57 (1.57/0.94/0.06)
W1	1°/12°	Chi	Rtopo2	d/o = 1024	100	2.5×10^4	3.75/5.03	2.75 (0.91/0.79/1.04)
W2	1°/12°	Chi	Rtopo2	d/o = 1024	175	1×10^4	4.18/5.39	2.58 (0.92/1.09/0.56)
W3	1°/12°	Chi	Rtopo2	d/o = 1024	None	4.5×10^4	8.03/9.74	2.96 (1.14/0/1.82)
R1	1°/3°	Chi	Rtopo2	d/o = 256	100	5.5×10^4	7.95/8.07	2.52 (0.80/0.95/0.77)
R2	1°/6°	Chi	Rtopo2	d/o = 512	100	3×10^4	5.21/5.95	2.58 (1.00/0.85/0.72)
WE	1°/12°	Arc	Gebco[d]	$\epsilon = 0.1$	None	4.5×10^4	15.39/17.85	3.50 (1.26/0/2.24)

Note. The individual experiments highlight the impact of several updated tidal processes and parameters on the achieved accuracy (P: pole-position; B: bathymetric map; S: SAL-scheme; W: topographic wave drag; R: resolution). Balances sometimes do not check out due to individual rounding.
[a]open ocean/tide gauge rms. [b]Tidal power consumption W and dissipation by sinks ($D_{bf}/D_{wd}/D_{ed}$, after Section 6). [c]Dissipation might be diminished as dissipative processes in the pole cap remain unresolved. [d]First order conservative remapping.

As an additional benchmark for our model we monitor planetary dissipation conducted by the M_2 tide. Being laid out by Platzman (1984), the theory of planetary dissipation was employed by Egbert and Ray (2000) and Egbert and Ray (2001) to derive estimates of M_2-tidal dissipation utilizing altimetry data-constrained tidal models. Herein, the planetary dissipation field d was derived by evaluating the relation

$$d = w - \nabla \mathbf{p}, \tag{14}$$

that uses the mean tidal energy consumption field $w = \rho_{sw}\langle \boldsymbol{a}_c \cdot \boldsymbol{v}\, H\rangle$ (work done by tidal forces) and the energy flux field $\nabla \mathbf{p} = \rho_{sw} g \nabla \langle \zeta H \boldsymbol{v}\rangle$. These studies revealed that 25%–30% of global M_2 dissipation $D_{M_2} = \int_S dA\, d \approx 2.45\,\mathrm{TW}$ is located in the deep ocean. Monitoring these properties can give further insight into the quality of a numerical model. Within this study, individual contributions to the planetary dissipation field $d = \sum_i d_i$ can be directly computed from the model, with $d_i = \rho_{sw}\langle \boldsymbol{a}_i \cdot \mathbf{v} H\rangle$ ($[d_i] = \mathrm{W}/m^2$), where a_i are individual dissipation accelerations mentioned in Equation 12. Globally integrating the individual fields d_i yields the corresponding planetary dissipation rates D_i ($[D_i] = \mathrm{W}$). Since temporal averages of dissipation terms originating from linear forces can be calculated easily ($\overline{\sin \omega t^2} = 0.5$) we calculate the nonlinear dissipation by bottom friction as the residual dissipation evaluating $D_{bf} = (W - D_{wd} - D_{ed})$, where W is the tidal power consumption w caused by $a_c = -g\vec{\nabla}(\zeta_{SAL} + \zeta_{eq})$. This does not introduce a bias into the estimates as the imbalance between tidal energy consumption and dissipation is far below $1\,\% D_{M_2}$ after initializing the simulation. The following subsections present the results obtained from tuning and sensitivity experiments and relate to the experiments summarized in Table 2.

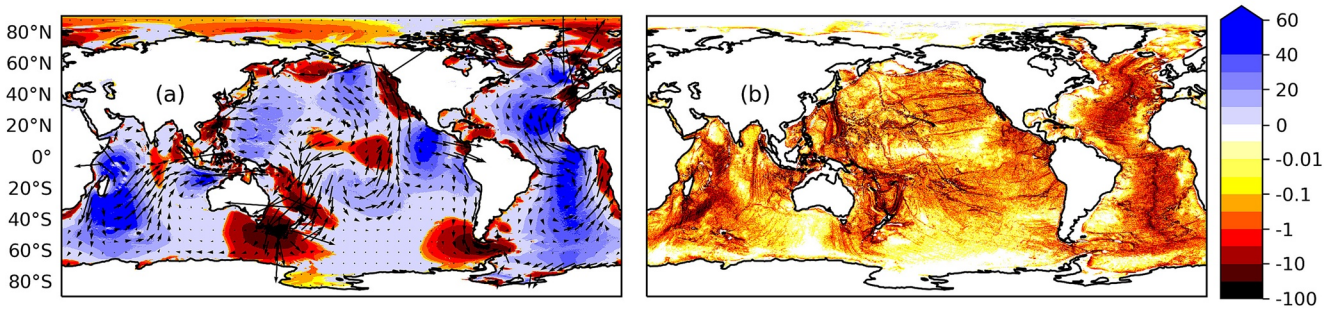

Figure 2. (a) Mean tidal power consumption field w overlayed with the tidal energy flux vector field $\mathbf{p}$ and (b) corresponding wavedrag dissipation field d_{wd} in $\frac{mW}{m^2}$. Red areas in subfigure (a) indicate regions, where water masses experience a net slow down by tidal forces. While energy fluxes are similar to those obtained by assimilating models (compare e.g., Egbert & Ray, 2001), deep ocean dissipation is concentrated at strong bathymetric slopes. Note that the scale was truncated at $+60\frac{mW}{m^2}$ and extended pseudologarithmically for values smaller than $-0.001\frac{mW}{m^2}$ to emphasize the underlying fine structured dissipation patterns.

6.1. Model Tuning

The original experiments conducted by Weis et al. (2008) (experiment WE in Table 2) led to an open ocean rms of 15.39 cm. The dissipation-rate was overestimated by 43% (1,050 GW) and strong concentration of dissipation in shallow waters indicated missing or not optimally represented dissipation mechanisms.

Primarily the introduction of topographic wave drag and an improved bathymetric map allowed to decrease global M_2 amplitudes and dissipation rates. Tuning experiments concentrated on finding an optimal ratio between damping by eddy viscosity and topographic wave drag, while the bottom friction was left constant at $r = 0.003$. Even though the original Nycander scheme does not contain a free, tunable parameter, experiments with $\kappa = 100\%$ showed that additional dissipation is necessary to obtain optimum results as was also found by Buijsman et al. (2015). This can either be provided by increasing A_h or κ (altering r worsened the accuracy). Several tuning experiments with $\kappa = 100...225\%$ and $A_h = 5...350 \cdot 10^2 \frac{m^2}{s}$ led to a minimum open ocean rms of 3.39 cm(experiment RE, tide-gauge rms: 4.83 cm, shallow water rms: 17.95 cm) with similar combinations of κ and A_h leading only to slightly higher rms-values (experiments W1,W2). While wavedrag dissipation amounts to 34% (910 GW) of the overall dissipation, the planetary dissipation rate decreased to 2.70 TW, which is still 10% (250 GW) too high compared to the expected result of 2.45 TW. The resulting mean tidal power consumption field w as well as the energy dissipation field by wavedrag-acceleration d_{wd} (see Figure 2) match the results derived with altimetric data (compare Egbert and Ray [2001]).

While the achieved accuracy of experiment RE was the highest in our ensemble, this model setup lacks a solid physical foundation due to the excessive dissipation mediated by parameterized eddy-viscosity. A physically more reasonable setting can be obtained when minimizing the dissipation by eddy-viscosity as pursued by most modern barotropic models (e.g., Egbert et al., 2004; Schindelegger et al., 2018). The obtained open ocean rms-values of 4.03/6.54 cm for W0 increase with respect to setting RE, while the dissipation-overshoot is reduced to 120 GW (5%). On the other hand, the shallow-water accuracy is not altered considerably to 17.86 cm. This can be seen as a trade-off between maximized model accuracy and well-founded model physics that will be beneficial with respect to sensitivity studies (e.g., paleo simulations, climatic impacts). On the other hand, this trade-off is undesirable for high-precision applications such as satellite gravimetry. As the accuracy that has to be sacrificed with setting W0 increases for minor tides (see Section 7), we decide to favor setting RE for the present study.

The amphidromic system and global rms-data for experiment RE is shown in Figure 3. In comparison to FES2014-data, M_2 oscillation systems are predicted precisely with exception of some features around Antarctica (compare Figure 5, top). It is worth noting that the reproduction of large-scale features (e.g., tidal phases defining amphidromic systems) was also possible on a similar level of detail by experiment WE. Exceptions were mainly constituted of bathymetry-induced aberrations around Antarctica (compare Section 6.3). The principal accuracy gain is attributed to a more realistic representation of dissipation, bathymetry, and

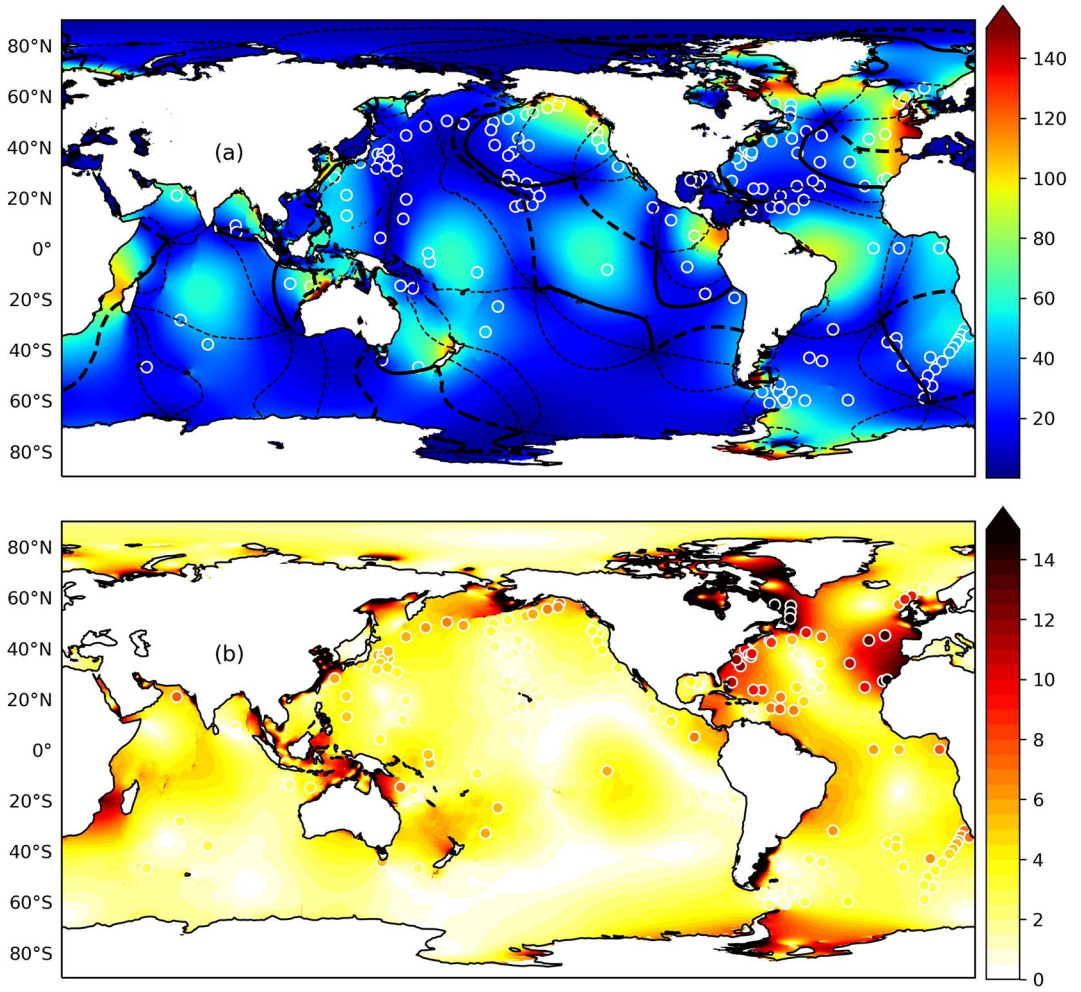

Figure 3. (a) TiME M_2 co-tidal chart in cm (experiment RE) augmented with tidal amplitudes at tide gauge stations (151 stations, small circles), where lines indicate the tidal phases in increments of 60° (Thick: 0°, Thick, Dashed: 60°). Further, validation results, expressed as rms (cm) between TiME and tidal constituents at tide gauge stations and FES2014-data are shown (b).

SAL effects. The remaining critical regions are shelf and coastal areas and especially concentrated around Antarctica and in the North Atlantic shelf areas. This suggests possible origins for these discrepancies in tide-ice interaction as well as in possible bathymetric inaccuracies or insufficient representation of (nonlinear) shallow water effects. With respect to similar modern barotropic tidal models, TiME produces solutions on the same level of accuracy, while the shallow water accuracy is moderately decreased (e.g., +4.4 cm to Schindelegger et al. (2018).

6.2. Impact of Pole Location

As a first finding we note similarly accurate results when performing experiments on alternative grids with land-covered poles (compare experiment P2 in Table 2). The accuracy obtained on the Gre-grid could be increased further to 3.63/5.00 cm open ocean rms, when additional tuning was applied (experiment P2b). Since the zonal model-resolution increases toward the numerical poles, the bathymetric information contained in two differently oriented grids differs slightly. This also impacts the wave drag tensor that depends on $H(\phi, \lambda)$. Together, this induces deviations between otherwise identical experiments performed on different grids (P2 vs. RE) that become more prominent when choosing coarser resolutions. Directly comparing the tidal elevations obtained by experiments RE and P2b (land covered poles), yields an open ocean $\overline{rms}$

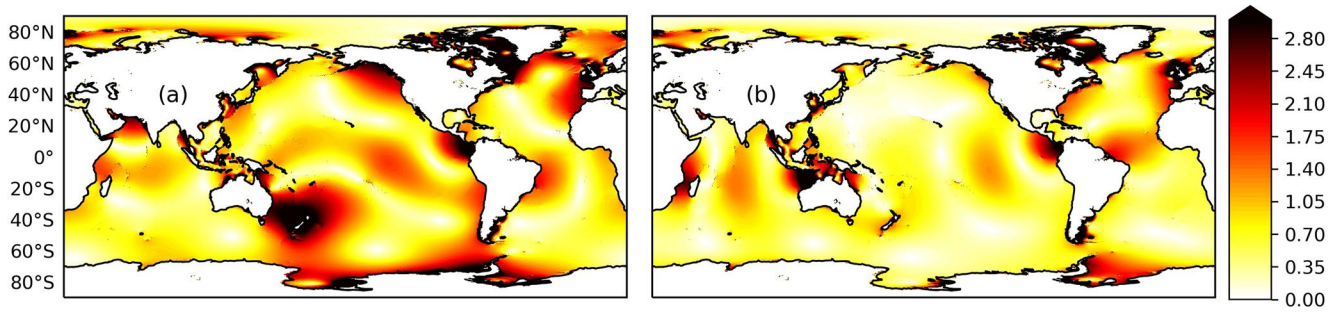

Figure 4. Rms-values obtained by intercomparing experiment RE to P2 (a), an experiment run with identical parameters on a different grid, versus a comparison between RE and P2b (b), where parameters have been readjusted. The open ocean $\overline{rms}$ amounts to 1.18/0.9 cm (a/b), while the shallow water rms is 5.46/5.35 cm. Note the different structures of shallow water residuals in comparison to Figure 3b, and the reduced scale.

of 0.90 cm, while only 5.35 cm are obtained in shallow waters (entire ocean: 1.97 cm) (compare Figure 4). These values estimate the effective precision level, that can be obtained when running experiments at the present resolution of $\frac{1^\circ}{12}$. We conclude that optimized parameters vary for experiments on differently oriented grids, but similar accuracy is achievable.

Overall, the rotated pole scheme did not improve the global accuracy level of present-day tides significantly, since tidal elevations in the Arctic (near to the former pole cap) are diminutive (experiment P1). Nevertheless, deviations induced by a pole cap situated in an area of presumably high tidal elevation are a source of imprecision (P3) and should be avoided. The non-optimally placed pole cap on the "Aus"-grid resulted in altered and diminished dissipation as well as in an increased $\overline{rms}$ = 4.75 / 5.57 cm.

An additional benefit of the implemented pole-rotation scheme lays in its versatility: The mitigation of the large pole-cap grid cell allows the unbiased study of historical situations in which tidal elevations in the Arctic might have been significant, as proposed by Griffiths and Peltier (2008) and more recently by Velay-Vitow et al. (2020) for the Last Glacial Maximum. Additionally, alternative grid orientations can be used to guarantee approximately equal aspect ratios for grid-cells in the Arctic (e.g., when using the Chi-grid), further recommending TiME to be used for studies of Arctic tides.

6.3. Impact of Bathymetry

Additional experiments were performed with bathymetries constructed from Etopo1 (Amante & Eakins, 2009) and Gebco data (GEBCO Compilation Group, 2019) treating sub-ice-shelf cavities as dry grid-cells. This configuration resembles the bathymetric maps used in Weis et al. (2008). Interpolation to the model's resolution was done using first-order conservative interpolation.

The results (experiment B1, B2) show that ignoring the effects of Antarctic sub-shelf cavities on ocean tide resonances leads to large scale deviations of the displayed amphidromic systems, especially in the southern ocean (Wilmes & Green, 2014) (compare Figure 5). The most striking deviation hereby occurs in the Weddell-Sea. As the Rtopo2-bathymetry is mainly based on Gebco-data, the model setup for experiment B1 can be seen as a blocking experiment for the Antarctic shelf regions. Blocking experiments are useful to investigate the back-action of shelf-tides on open ocean tides. Arbic, Karsten, and Garrett (2009) conducted such simulations for a number of shelf areas (e.g., Patagonian Shelf, Hudson Bay) and also considered analytical solutions. Both approaches predict that blocking a near-resonant shelf-region enhances the amplitude of the open ocean tide, as it is shown in Figures 5a and 5c for the Southern Ocean. As the shelf-blocking increases the open ocean amplitudes, tidal dissipation is also increased and contributes to the overestimated dissipation in experiment WE (B1: +150 GW, B2: +350 GW). It is possible to reduce this overestimation slightly by enhancing the dampening forces. However, this only leads to minor improvements and cannot rectify the imprecisely represented oscillation systems as depicted in Figure 5, it is therefore not further investigated.

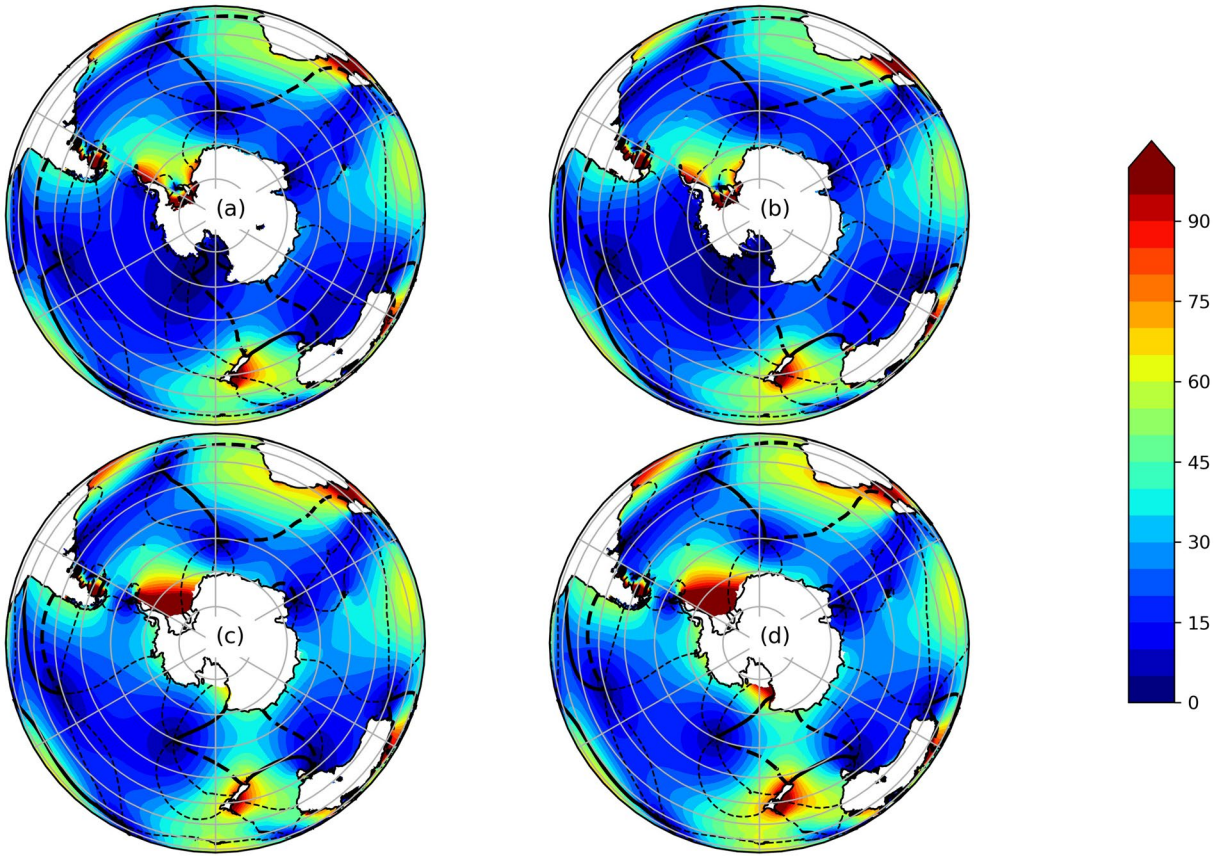

Figure 5. M_2-Tidal elevations (cm) and phase-lags (compare Figure 3) around Antarctica obtained from TiME-simulations with different bathymetric charts: (a) Rtopo2 (experiment RE), (c) Gebco (experiment B1), and (d) Etopo1 (experiment B2). As a reference (b) shows FES2014 tidal elevations. Note the hydrodynamically blocked sub-shelf cavities for the bottom experiments.

In summary, the conducted experiments highlight the irreplaceability of constructing a realistic bathymetric map. Further, the results point out that poorly represented areas can have strong near- and far-field effects on tidal dynamics even if they have only a small spatial extent.

6.4. Impact of SAL

In this section, we discuss the impact of a number of SAL representations on the simulation results. When evaluating Equation 10 up to $l_{max} = 100$ we find that the open ocean rms does not increase indicating sufficient handling of this effect with regard to open ocean tidal dynamics (experiment S1). The shallow water rms is also not altered considerably, which might be due to a generally less precise model performance in shallow waters. When further decreasing the maximum degree to $l_{max} = 10$ the open ocean rms increases to 3.99/5.63 cm (S2) which is still a significantly more precise result than S3, that was obtained by the local SAL-parametrization by (Accad & Pekeris, 1978) (5.41/6.69 cm). However, this result can be seen as a valuable improvement when comparing it to completely neglecting the effect (experiment S4). This leads to profound misrepresentation of tidal phases and strongly increased misfit. Overall, the estimated planetary dissipation increases with a less precise SAL representation (S3: +240 GW, S4: +500 GW). Thus, the local SAL-parametrization contributes significantly to the overestimated dissipation in experiment WE.

As discussed by Müller (2007) the inclusion of SAL primarily leads to a phase-shift of oscillation systems by altering properties of the underlying normal modes. This phase shift is well approximated in first order by applying an effectively reduced gravity factor (S3). However, to represent the precise far-field effects of the SAL a treatment in terms of spherical harmonics with $l_{max} \geq 100$ is necessary. To precisely represent near field effects the maximum degree l has to be extended to higher values (Schindelegger et al., 2018). Since the

efficient handling of SAL-transformation by the SHTNS-package (Schaeffer, 2013) does not considerably increase computation time we treat the SAL effect up to degree $l_{max} = 1{,}024$ in our experiments.

6.5. Impact of Topographic Wave Drag

The only dissipation channel that leads to considerable deep ocean dissipation included in the model is the excitation of internal tides by topographic effects. Since deep ocean dissipation is an experimental matter of fact, it does not surprise that complete neglection of this effect has severe impacts on the achievable accuracy (experiment W3) causing an rms increase of +4.64/+4.91 cm and a surplus dissipation of an additional 260 GW. Finding an optimum interplay between the present dissipation channels on the other hand is more complicated. When abstaining from tuning wave drag-strength, e.g., setting $\kappa = 100\%$, best results are achieved by allowing significant dissipation by eddy-viscosity (W1). If one instead decides to increase wave drag substantially (W2), as for example, done by Buijsman et al. (2015), the open ocean results slightly worsened in comparison to experiment RE, without improving shallow water rms. As discussed in Section 6.1 a minimization of the obtained wavedrag dissipation leads to the physically well-founded model setting W0 while the open ocean accuracy moderately deteriorates (+0.64/1.71 cm). This setting should always be favorable with respect to sensitivity experiments that benefit from realistically represented tidal physics.

Overall the tuning of the dissipation channels suggested that best results are obtained when wavedrag dissipation contributes about 900 GW to planetary dissipation, which is close to the expected value. The slight tuning of the wave drag tensor (factor 1.25 to the original Nycander-tensor) stresses that it is based on a reliable theoretical basis and can be expected to provide ad-hoc precise results. This is a valuable result when it comes to adapting the model to other tidal groups or paleo settings.

6.6. Impact of Spatial Resolution

Experiments R1 $\left(\text{at } \frac{1^\circ}{3}\right)$ and R2 $\left(\text{at } \frac{1^\circ}{6}\right)$ were designed to represent a similar physical situation as chosen for experiment RE. Therefore, dissipation channels were tuned to achieve comparable dissipation ratios leading to an effective increase in A_h. We emphasize, that altering the model resolution renders repeated model tuning necessary. Parameters cannot be transferred directly without altering tidal dynamics.

We observe that, while overall dissipation decreases, open ocean $\overline{rms}$-values are considerably increased to 5.21/7.95 cm for R2/R1 (compare Egbert et al. [2004]). The cause for this might originate from the model-inherent resonant behavior of oceanic tides. With reduced spatial resolution, the geometry of the ocean basins determining oceanic normal-modes cannot be properly represented. The resulting slight shifts in resonance frequencies then strongly impact tidal dynamics, especially in shallow waters, where oscillation systems reside on smaller spatial scales. Thus, to further increase the precision and accuracy of TiME, an increased resolution beyond $\frac{1^\circ}{12}$ should be considered.

7. Additional Tidal Excitations

In this section, we present simulation results for additional partial tides. We selected partial tides that differ in excitation amplitude, frequency as well as in excitation pattern from M_2 to test the sensitivity of the preferred model setting RE. The overall aim is to demonstrate model setting RE as robust for simulating partial tides of differing character on a comparable level of accuracy.

As discussed in Section 3, excitation patterns relate to the spatial dependence of the partial tide forcing that is proportional to the spherical harmonic functions Y_{lm}. Within, l defines the degree, m the order of the spherical harmonic function, where $m = 0, 1, 2, 3$ further enumerates the tidal species (0: long period, 1: diurnal, 2: semidiurnal, 3: terdiurnal). Since the tidal forcing strength spans several scales for different partial tides, the level of accuracy obtained for different partial tides cannot be compared directly to each other without considering the overall signal amplitude.

To facilitate this comparison we introduce the admittance function

$$Z_{lm}(\mathbf{x},\omega_i,\mathrm{amp}(\omega_i)) = \frac{\zeta^{\omega_i}(\boldsymbol{x})}{\mathrm{amp}(\omega_i)} g\,, \tag{15}$$

that relates the tidal response, expressed by its elevation ζ^{ω_i}, to its g-normalized forcing amplitude $\mathrm{amp}(\omega_i) = \sqrt{(S_i^{lm})^2 + (C_i^{lm})^2}$ (compare supporting information). Hereby, Z_{lm} is only evaluated at discrete tidal frequencies for partial tides with forcing pattern Y_{lm}. Since the tidal PDEs are only weakly non-linear and tidal frequencies within one tidal band only differ slightly, Z_{lm} takes a related shape for each partial tide. Hence, it can be used to compare the response strength and especially the relative level of accuracy compared to the excitation strength for individual excitations by considering $rms_{Z^{\omega}_{TiME}, Z^{\omega}_{FES}}(\mathbf{x})$ (compare Equation 13). Please refer to the supporting information where the tidal potential catalog used for this study can be obtained.

7.1. Semidiurnal Tides

The K_2-excitation is a semidiurnal partial tide of second degree origin ($l = 2$), thus representing another evaluation point of admittance function Z_{22}. However, its respective forcing strength is only approximately 13% compared to M_2. Since additionally its frequency differs from M_2 by $1.10\frac{^\circ}{h}$, admittance patterns are altered in comparison to M_2. The open ocean validation for K_2 results in an $\overline{rms}$ of 0.39/0.43 cm. Compared to K_2 signal strength, the obtained accuracy is on the same level of accuracy as results for M_2. In other words, the uncertainty in Z_{22} is similar for both partial tides.

Further, we considered the tidal response to ν_2 tide (approx. 4% M_2-forcing) as a third evaluation point of Z_{22}. Here, nonlinear effects will play an even more important role, due to the diminished excitation amplitude, while frequency difference to M_2 is reduced $\left(\delta\omega = 0.47\frac{^\circ}{h}\right)$. The validation of ν_2 resulted in a $\overline{rms}$ of 0.19/0.18 cm, revealing a moderately enhanced level of inaccuracy compared to K_2-results. The reason for this could be found in an imperfect representation of non-linearities in tidal dynamics. Nonetheless, the results demonstrate that TiME is able to perform simulations on a similar scale of accuracy within one tidal band (in this case Z_{22}) without the need to adapt model parameters for each simulation. Results for these partial tides are shown in Figure 6.

On the other hand, monitoring tidal dissipation reveals increasingly altered weights for individual dissipation channels. While K_2 dissipates 34.7 GW, partitioning as (D_{bf}, D_{wd}, D_{ed} = 4.9/13.6/16.3 GW) the distribution for ν_2 (D_{bf}, D_{wd}, D_{ed} = 0.34/1.33/2.21 GW) is even more shifted toward a dominant eddy-dissipation. Not surprisingly, the dissipation by quadratic bottom friction $\sim|v|^3$ is strongly reduced compared to dissipation by linear forces $\sim|v|^2$. Remarkably, the overall dissipation lost by reduced bottom friction is transferred to D_{ed}, while deep ocean dissipation by D_{wd} amounts to a comparable fraction (33.6/38.4/34.2% for $M_2/K_2/\nu_2$) of dissipation.

On the other hand, simulation results obtained with model setting W0 (compare Table 3) reveal decreasingly accurate results for minor tides. While for M_2 the decrease of open ocean accuracy was at a moderate level of 19% the toll for implementing setting W0 increases by 54 (84)% for the K_2 (ν_2) excitation. The reason for this could reside in a possible overestimation of quadratic (non-linear) shelf-dissipation mechanisms when adapting the setting W0 for the M_2 tide. The importance of a nonlinear dissipation channel (quadratic bottom friction) reduces strongly for minor tides, which could result in distorted ratios between deep ocean and shelf-dissipation. As the accentuation of an alternative linear dissipation mechanism (eddy-viscosity) in model setting RE improves the results for minor tides drastically, it could be beneficial to consider novel linear shelf-dissipation mechanisms for the precise prediction of minor tides. In spite of the poor physical justification of dominant eddy-dissipation it might thus be its linear nature that benefits the accuracy of hydrodynamical tidal simulations.

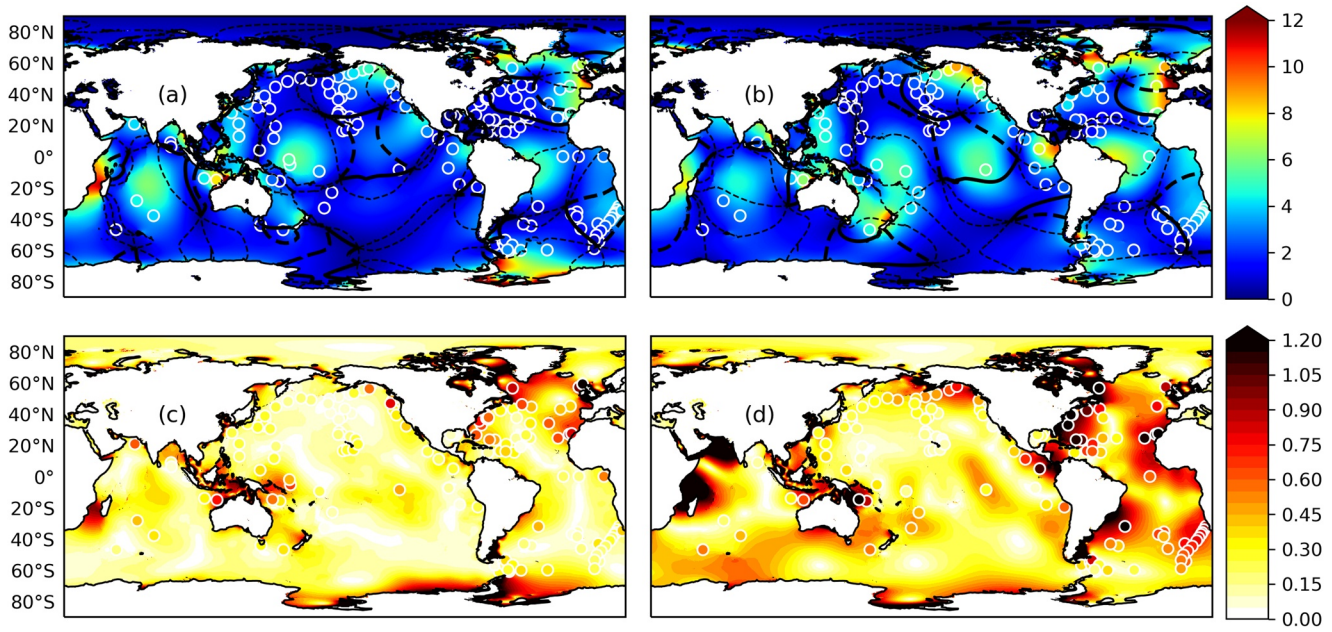

Figure 6. Dimensionless admittance-function Z_{22} for K_2- (a) and ν_2 tide (b) and corresponding rms-values for Z_{22} (c + d). Note that the scales of the colorbars correspond to Figure 3, saying that Figure 3 can be read as $Z_{22}(M_2)$. Rescaling Z_{22}-amplitudes to real ocean elevation amounts to 19.10/5.50 cm for K_2/ν_2.

7.2. Diurnal Tides

The K_1 tide is the principal excitation in the diurnal band with a magnitude of 58% M_2-forcing strength. It is important to note that the resulting forcing applied on ocean masses is enhanced by 6.2%, compared to an equivalent forcing at semidiurnal frequencies due to the NDFW-resonance (compare Table 1). In contrast to Z_{22}, the tidal excitation pattern is proportional to Y_{21} and the strongly dispersive wave drag-parametrization is further limited to low latitudes with $|\Phi| < 30°$. This causes the admittance function Z_{21} to take a different shape compared to Z_{22}. Tidal elevations are now concentrated in the North Pacific, Indian, and Southern Ocean. Validation performance yields an $\overline{rms}$ of 0.90/1.32 cm (compare Figure 7). A possible explanation for the overall higher accuracy might be the larger scales of diurnal oscillations systems, that are less sensitive to detailed bathymetric information. Moreover, the overall smaller admittance in the diurnal tidal band (Z_{21}) indicates less resonant tidal behavior, and thus, less sensitivity to slight changes. We further display a second diurnal oscillation system (Q_1) to demonstrate the achieved accuracy over multiple scales of excitation amplitude. While the forcing-strength is reduced by 86.4% compared to K_1, validation accuracy is on a similar level, yielding 0.19/0.25 cm open ocean rms. Due to the shift in excitation frequency by $1.70\frac{^\circ}{h}$, the admittance-function Z_{21} changes notably. This also leads to an altered concentration of uncertainty in (shelf)-regions.

Concluding this chapter, we want to stress that the achieved high accuracy for 5 partial tides of diverse character proves the model setting RE as suitable and favorable over other settings for high accuracy applications.

Table 3
Model Accuracy as Measured by Open Ocean Rms/Tide Gauge Rms (Compare Section 6) for the Discussed Ensemble of Semidiurnal Partial Tides (M_2, K_2, ν_2) as Obtained by the Default Setting RE and Setting W0

Partial tide	M_2	K_2	ν_2
Rms (cm), RE	3.39/4.83	0.39/0.43	0.19/0.18
Rms (cm), W0	4.03/6.54	0.60/0.64	0.35/0.40

8. Tidal Solutions for Satellite Gravimetry

In the previous section, it was shown that with model setting RE it is possible to simulate minor tides at a similar level of relative accuracy for a wide range of tidal frequencies, excitation amplitudes, and excitation patterns. On the other hand, the precision of satellite data-constrained partial tide solutions depends on the available data quality. This quality is not constant but depends on the respective frequency and domain of tidal observations. Typically, polar tides are less accurately known since many

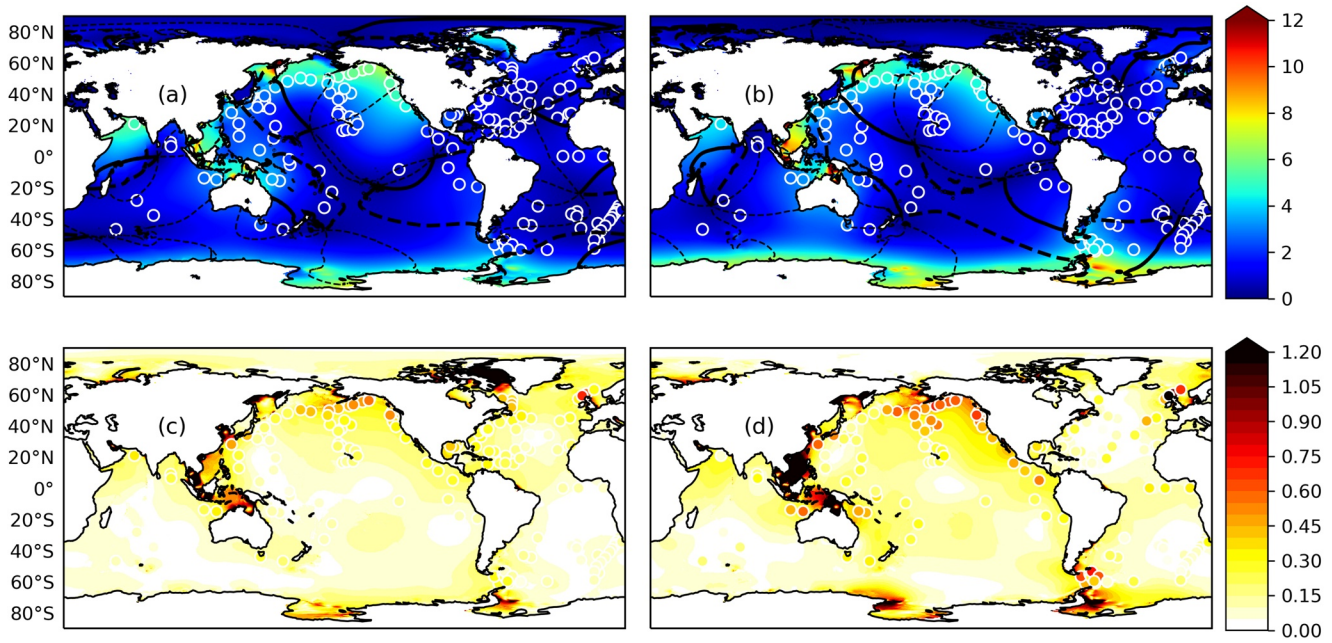

Figure 7. Dimensionless admittance-function Z_{21} for K_1- (a) and Q_1 tide (b) and corresponding rms-values for Z_{21} (c + d). Rescaling Z_{21} to real ocean elevations amounts to 88.14/12.00 cm for K_1/Q_1. Note the overal lower response level compared to Z_{22} (Figures 3 and 6).

satellite orbits are limited to $|\phi| < 66°$. This leads to prominent GRACE residuals (Ray, Loomis, et al., 2019; Ray, Luthcke, & Boy, 2009; Wiese et al., 2016) in polar seas. The same is true for minor tidal constituents that are routinely considered for gravity field de-aliasing (Savcenko & Bosch, 2010), but are often not provided explicitly by data-constrained tidal atlases as the data quality is poor. As this might change at sometime with continuously extended altimeter time-series (Ray, 2020), minor tides are currently routinely derived by admittance assumptions (Gérard & Luzum, 2010), that are prone to reduced accuracy especially in shallow waters and ice shelf regions (e.g., Pedley et al., 1986) that are governed by nonlinear processes. In this framework, it is natural to ask if purely hydrodynamic solutions can perform more accurate than data-constrained solutions. While this is certainly not true for major constituents (M_2, K_1, ...) we want to take a closer look at minor tidal constituents, that are yet relevant for gravity field de-aliasing.

Most promising results can be expected by tides at the edges of tidal bands, as these contain the potentially largest errors when utilizing linear admittance theory (Ray, Luthcke, & Boy, 2009). Thus, we choose the diurnal $2Q_1$ and OO_1 tides (1.0%/1.8% M_2-forcing strength) as first test cases. The validation is performed with a set of tide gauges stations of predominantly coastal character (TICON, Piccioni et al., 2019). Additionally, we probe Q_1-results in the Antarctic region by validation with a data set of Antarctic tide gauges stations (Howard & Padman, 2020). The respective solutions are either directly included in the FES2014-atlas (Q_1), or derived via linear admittance supported by Q_1, O_1- and K_1 tide, where we consider perturbations in the tidal potential height by the NDFW-resonance (compare Tab. 1). Hereby we assume $\partial_\omega Z_{lm} = c_1 + c_2\omega$ (compare Equation 15), evaluate the constants c_1, c_2 by the two closest supporting points and use the result to extrapolate the results linearly to $2Q1$ (support Q_1, O_1) and OO_1 (support O_1, K_1).

As the distribution of the respective rms-values is considerably askew, especially for the TICON-dataset (compare Figure 8), we decided to utilize the distribution median as an effective validation metric. The median will be listed in the following for the (TiME/FES2014)-distributions. TiME performs on a similar level of accuracy as FES2014 for Q_1 in the Antarctic domain (1.04/0.83 cm). While this is already quite remarkable for an unconstrained model, it proposes that the local, nonlinear particularities of tides below ice shelves must be considered explicitly to obtain more accurate results. On the other hand, the accuracy for $2Q_1$ (0.07/0.11 cm) and even more for OO_1 (0.17/0.34 cm) is clearly increased when TiME solutions are employed. From this improvement of validation accuracy with respect to linear admittance solutions, we draw the conclusion that the utilization of TiME-solutions for certain partial tides will result in a reduction

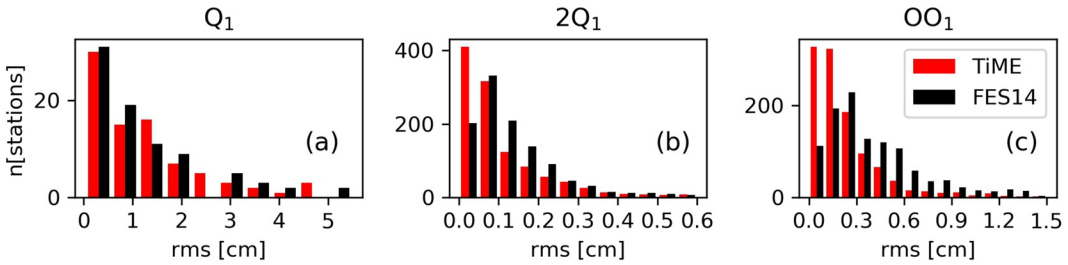

Figure 8. Respective rms-distributions for the $Q1$ tide (Antarctic TGs, a), the $2Q_1$ tide (TICON, (b) and the OO_1 tide (TICON, (c).

of the aliased tidal signal in GRACE-data. This de-aliasing potential for GRACE-data exhibited by our minor tide solutions emerges from the integrated improvement of the model and its high accuracy over a wide range of partial tide.

9. Summary and Outlook

In this paper, we introduced several modifications to the barotropic tidal model TiME (Weis et al., 2008), which resulted in a considerable increase of the open ocean accuracy.

First, we showed that the introduction of a comprehensive pole rotation scheme allows us to get rid of numerical artifacts potentially induced by the former pole cap handling. The realization of two "pari passu" grid orientations with land-covered numerical poles further allowed to estimate resolution-connected model uncertainties.

Second, the introduction of a non-local online treatment of the effect of SAL (Ray, 1998) and the implementation of a wave drag-parametrization (Nycander, 2005) allowed for a substantial increase in the model accuracy. We further discussed the relevance of constructing optimized bathymetric maps from different available global data sets. The resulting update on TiME's bathymetry evoked another significant increase in model accuracy, especially due to the inclusion of sub-ice-shelf cavities (Wilmes & Green, 2014). The individual contributions of these updates to model accuracy are summarized in Table 4.

Due to the removal of the numerical pole cap, TiME proved to be highly versatile in simulating arbitrary oceanic regions with the same level of accuracy. An open question is the correct representation of (nonlinear) processes in shallow water, beneath ice shelves, and coastal areas, where the model accuracy considerably drops. Though dissipation by eddy-viscosity (a linear dissipative force) increased the overall model accuracy considerably, the obtained high values for A_h are hard to justify. The question of shallow-water dissipation should be readdressed, also given the persistently overestimated M_2-tidal dissipation.

Tuning experiments of the updated model resulted in a set of model parameters, that equally distributes M_2 tidal dissipation to friction by wave drag, quadratic bottom-turbulence, and parametrized eddy-viscosity. The set of model parameters proved robust toward the simulation of diurnal tides and minor tidal excitations, where results with comparable relative accuracy were obtained. On the other hand, parameters had to be adjusted slightly, when changing the model's resolution. While the discussed setting is favorable for the gravimetric applications we are envisioning, a second, physically better-founded setting was derived, that is favorable for sensitivity studies, or paleo experiments.

The achieved model performance qualifies TiME as a purely hydrodynamic tidal model for simulation of modern-day tides. While absolute model deviations from tide gauge data are considerably bigger than results obtained by data-constrained tidal models for major tides, we could show that the accuracy for minor tides can be improved. The same might be possible for polar tides of major origin if crucial polar tidal processes as sea-ice-friction are considered. This potential arises from TiME's

Table 4
Rms-Increase $\Delta\overline{rms}$ Measured by Open Ocean and Tide Gauge Metrics, When Diverging From the Default Setting (Experiment RE)

Setting	No wave drag	Bathymetry[a]	Param. SAL	Bad pole cap
Experiment	W3	B1	S3	P3
$\Delta\overline{rms}$ [cm]	+4.64/4.91	+3.10/2.52	+2.02/1.86	+1.36/0.74

[a]Deviations mainly due to blocked ice-shelf cavities.

independence off satellite data and allows for an almost constant relative model accuracy over multiple scales in tidal forcing strength. To fully benefit from the de-aliasing potential of the obtained solution a comprehensive study focusing on the accuracy improvement of all relevant minor tides by unconstrained simulations should be conducted and augmented with direct estimates of GRACE-gravity field solutions.

Data Availability Statement

The tidal data presented in this study can be obtained from https://doi.org/10.5880/GFZ.1.3.2021.001 in the form of Stokes coefficients including load-tide mass variations (Sulzbach et al., 2021).

Acknowledgments
The authors sincerely thank the editor Don Chambers and the anonymous reviewers for their very constructive comments and suggestions regarding our manuscript. The authors acknowledge funding by the NEROGRAV-project (DFG Research Unit 2736, Grant: TH864/15-1). This work used resources of the Deutsches Klimarechenzentrum (DKRZ) granted by its Scientific Steering Committee (WLA) under project ID 499.

References

Accad, Y., & Pekeris, C. (1978). Solution of the tidal equations for the M_2 and S_2 tides in the world oceans from a knowledge of the tidal potential alone. *Philosophical Transactions of the Royal Society of London. Series A*, *290*(1368), 235–266. https://doi.org/10.1098/rsta.1978.0083

Agnew, D. C. (2007). Earth tides. In Treatise on geophysics: Geodesy (Vol. 3, pp. 163–195). Elsevier. https://doi.org/10.1029/RG013i003p00260

Amante, C., & Eakins, B. (2009). *ETOPO1 1 Arc-Minute Global Relief Model: Procedures, data sources and analysis*. NOAA Technical Memorandum NESDIS NGDC-24. National Geophysical Data Center. https://doi.org/10.7289/V5C8276M

Arbic, B. K., Karsten, R. H., & Garrett, C. (2009). On tidal resonance in the global ocean and the back-effect of coastal tides upon open-ocean tides. *Atmosphere-Ocean*, *47*(4), 239–266. https://doi.org/10.3137/OC311.200910.3137/OC311.2009

Arbic, B., Richman, J., Shriver, J., Timko, P., Metzger, J., & Wallcraft, A. (2012). Global modeling of internal tides within an eddying ocean general circulation model. *Oceanography*, *25*(2), 20–29. https://doi.org/10.5670/oceanog.2012.38

Backhaus, J. O. (1985). A three-dimensional model for the simulation of shelf sea dynamics. *Deutsche Hydrographische Zeitschrift*, *38*, 165–187. https://doi.org/10.1007/bf02328975

Backhaus, J. O. (1983). A semi-implicit scheme for the shallow water equations for application to shelf sea modelling. *Continental Shelf Research*, *2*(4), 243–254. https://doi.org/10.1016/0278-4343(82)90020-6

Bartels, J. (1957). Gezeitenkraefte. *Handbuch der Physik*. Geophysik II (Vol 48, p. 525).

Bell, T. H. (1975). Topographically generated internal waves in the open ocean. *Journal of Geophysical Research*, *80*(3), 320–327. https://doi.org/10.1029/jc080i003p00320

Blewitt, G. (2003). Self-consistency in reference frames, geocenter definition, and surface loading of the solid Earth. *Journal of Geophysical Research*, *108*(B2). https://doi.org/10.1029/2002jb002082

Buijsman, M. C., Arbic, B. K., Green, J. A. M., Helber, R. W., Richman, J. G., Shriver, J. F., et al. (2015). Optimizing internal wave drag in a forward barotropic model with semidiurnal tides. *Ocean Modelling*, *85*, 42–55. https://doi.org/10.1016/j.ocemod.2014.11.003

Carrere, L., Lyard, F., Cancet, M., & Guillot, A. (2015). FES 2014, a new tidal model on the global ocean with enhanced accuracy in shallow seas and in the Arctic region. *EGU General Assembly Conference Abstract* (Vol. *17*, p. 5481). Retrieved from http://adsabs.harvard.edu/abs/2015EGUGA.17.5481C

Chen, J. L., Pekker, T., Wilson, C. R., Tapley, B. D., Kostianoy, A. G., Cretaux, J.-F., & Safarov, E. S. (2017). Long-term Caspian Sea level change. *Geophysical Research Letters*, *44*(13), 6993–7001. https://doi.org/10.1002/2017GL073958

Cheng, Y., & Andersen, O. B. (2011). Multimission empirical ocean tide modeling for shallow waters and polar seas. *Journal of Geophysical Research*, *116*, (C11), https://doi.org/10.1029/2011jc007172

Doodson, A. T. (1928). The Analysis of Tidal Observations. *Philosophical Transactions of the Royal Society of London, Series A, Containing papers of a Mathematical or Physical Character*, *227*, 223–279.

Dushaw, B. D., Egbert, G. D., Worcester, P. F., Cornuelle, B. D., Howe, B. M., & Metzger, K. (1997). A TOPEX/POSEIDON global tidal model (TPXO.2) and barotropic tidal currents determined from long-range acoustic transmissions. *Progress in Oceanography*, *40*, (1-4), 337–367. https://doi.org/10.1016/s0079-6611(98)00008-1

Egbert, G. D., & Erofeeva, S. Y. (2002). Efficient inverse modeling of barotropic ocean tides. *Journal of Atmospheric and Oceanic Technology*, *19*(2), 183–204. https://doi.org/10.1175/1520-0426(2002)019⟨0183:EIMOBO⟩2.0.CO;2

Egbert, G. D., & Ray, R. D. (2000). Significant dissipation of tidal energy in the deep ocean inferred from satellite altimeter data. *Nature*, *405*(6788), 775–778. https://doi.org/10.1038/35015531

Egbert, G. D., & Ray, R. D. (2001). Estimates of M2tidal energy dissipation from TOPEX/Poseidon altimeter data. *Journal of Geophysical Research: Oceans*, *106*, (C10), 22475–22502. https://doi.org/10.1029/2000jc000699

Egbert, G.D., & Ray, R. D. & Bills, B. G. (2004). Numerical modeling of the global semidiurnal tide in the present day and in the last glacial maximum. *Journal of Geophysical Research: Oceans*, *109*, (C3), https://doi.org/10.1029/2003jc001973

Einšpigel, D., & Martinec, Z. (2017). Time-domain modeling of global ocean tides generated by the full lunisolar potential. *Ocean Dynamics*, *67*(2), 165–189. https://doi.org/10.1007/s10236-016-1016-1

Flechtner, F., Neumayer, K.-H., Dahle, C., Dobslaw, H., Fagiolini, E., Raimondo, J.-C., & Güntner, A. (2016). What Can be Expected from the GRACE-FO Laser Ranging Interferometer for Earth Science Applications?. *Surveys in Geophysics*, *37*, (2), 453–470. https://doi.org/10.1007/s10712-015-9338-y

Fok, H. S. (2012). Ocean tides modeling using satellite altimetry (Technical Report) (Vol. 501). Ohio State University. https://doi.org/10.1017/CBO9781107415324.004

Fu, L.-L., & Cazenave, A. (2000). Satellite altimetry and Earth sciences (1st ed., Vol. 69). Academic Press.

GEBCO Compilation Group. (2019). *GEBCO 2019 Grid*. https://doi.org/10.5285/836f016a-33be-6ddc-e053-6c86abc0788e

Gérard, P., & Luzum, B. (2010). *IERS Conventions (2010)* (Technical Note No. 36) Bureau International des Poids et Mesures. Retrieved from https://www.iers.org/IERS/EN/Publications/TechnicalNotes/tn36.html

Ghobadi-Far, K., Han, S.-C., McCullough, C. M., Wiese, D. N., Yuan, D.-N., Landerer, F. W., et al. (2020). GRACE Follow-On Laser Ranging Interferometer Measurements Uniquely Distinguish Short-Wavelength Gravitational Perturbations. *Geophysical Research Letters*, *47*, (16), https://doi.org/10.1029/2020gl089445

Gooding, R. H., & Wagner, C. A. (2010). On a Fortran procedure for rotating spherical-harmonic coefficients. *Celestial Mechanics and Dynamical Astronomy*, *108*(1), 95–106. https://doi.org/10.1007/s10569-010-9293-3
Green, J. A. M., & Nycander, J. (2013). A comparison of tidal conversion parameterizations for tidal models. *Journal of Physical Oceanography*, *43*(1), 104–119. https://doi.org/10.1175/jpo-d-12-023.1
Griffiths, S. D., & Peltier, W. R. (2008). Megatides in the Arctic Ocean under glacial conditions. *Geophysical Research Letters*, *35*, (8), https://doi.org/10.1029/2008gl033263
Hartmann, T., & Wenzel, H.-G. (1995). The HW95 tidal potential catalogue. *Geophysical Research Letters*, *22*, (24), 3553–3556. https://doi.org/10.1029/95gl03324
Hauk, M., & Wiese, D. N. (2020). New Methods for Linking Science Objectives to Remote Sensing Observations: A Concept Study Using Single- and Dual-Pair Satellite Gravimetry Architectures. *Earth and Space Science*, *7*, (3), https://doi.org/10.1029/2019ea000922
Heiskanen, W. A., & Moritz, H. (1967). *Physical geodesy*. W. H. Freeman and Company.
Hendershott, M. C. (1972). The effects of solid Earth deformation on global ocean tides. *Geophysical Journal International*, *29*(4), 389–402. https://doi.org/10.1111/j.1365-246X.1972.tb06167.x
Hewitt, E., & Hewitt, R. E. (1979). The Gibbs-Wilbraham phenomenon: An episode in fourier analysis. *Archive for History of Exact Sciences*, *21*, (2), 129–160. https://doi.org/10.1007/bf00330404
Howard, S., & Padman, L. (2020). *Antarctic tide gauge database, version 1*. U.S. Antarctic Program (USAP) Data Center. https://doi.org/10.15784/601358
Hsu, P.-C., Lee, H.-J., Zheng, Q., Lai, J.-W., Su, F.-C., & Ho, C.-R. (2020). Tide-Induced Periodic Sea Surface Temperature Drops in the Coral Reef Area of Nanwan Bay, Southern Taiwan. *Journal of Geophysical Research: Oceans*, *125*, (4), https://doi.org/10.1029/2019jc015226
Kohyama, T., & Wallace, J. M. (2016). Rainfall variations induced by the lunar gravitational atmospheric tide and their implications for the relationship between tropical rainfall and humidity. *Geophysical Research Letters*, *43*(2), 918–923. https://doi.org/10.1002/2015GL067342
Kvas, A., Behzadpour, S., Ellmer, M., Klinger, B., Strasser, S., Zehentner, N., & Mayer-Gürr, T. (2019). ITSG-Grace2018: Overview and Evaluation of a New GRACE-Only Gravity Field Time Series. *Journal of Geophysical Research: Solid Earth*, *124*, (8), 9332–9344. https://doi.org/10.1029/2019jb017415
Llewellyn Smith, S. G., & Young, W. R. (2003). Tidal conversion at a very steep ridge. *Journal of Fluid Mechanics*, *495*, 175–191. https://doi.org/10.1017/s0022112003006098
Locarnini, R. A., Mishonov, A. V., Baranova, O. K., Boyer, T. P., Zweng, M. M., Garcia, H. E., et al. (2019). World Ocean Atlas 2018, Volume 1: Temperature. In A. Mishonov (Ed.), NOAA Atlas NESDIS 81 (Vol. 1, p. 52). Retrieved from http://www.nodc.noaa.gov/OC5/indprod.html
Love, A. E. H. (1909). The yielding of the earth to disturbing forces. *Proceedings of the Royal Society of London. Series A, Containing Papers of a Mathematical and Physical Character*, *82*, (551), 73–88. https://doi.org/10.1098/rspa.1909.0008
Luyten, J. R., & Stommel, H. M. (1991). Comparison of M2 tidal currents observed by some deep moored current meters with those of the Schwiderski and Laplace models. *Deep Sea Research Part A. Oceanographic Research Papers*, *38*, S573–S589. https://doi.org/10.1016/s0198-0149(12)80024-0
Lyard, F., Lefevre, F., Letellier, T., & Francis, O. (2006). Modelling the global ocean tides: modern insights from FES2004. *Ocean Dynamics*, *56*, (5-6), 394–415. https://doi.org/10.1007/s10236-006-0086-x
Maus, S. (2004). Ocean tidal signals in observatory and satellite magnetic measurements. *Geophysical Research Letters*, *31*, (15), https://doi.org/10.1029/2004gl020090
McDougall, T. J., & Barker, P. (2011). *Getting started with TEOS-10 and the Gibbs Seawater (GSW) Oceanographic Toolbox* (p. 28). SCOR/IAPSO WG127.
Melet, A., Nikurashin, M., Muller, C., Falahat, S., Nycander, J., Timko, P. G., et al. (2013). Internal tide generation by abyssal hills using analytical theory. *Journal of Geophysical Research: Oceans*, *118*(11), 6303–6318. https://doi.org/10.1002/2013JC009212
Müller, M. (2007). The free oscillations of the world ocean in the period range 8 to 165 hours including the full loading effect. *Geophysical Research Letters*, *34*, (5), https://doi.org/10.1029/2006gl028870
Munk, W. H., & MacDonald, G. J. F. (1960). *The rotation of the Earth*. Cambridge University Press.
Naderi Beni, A., Lahijani, H., Mousavi Harami, R., Arpe, K., Leroy, S. A. G., Marriner, N., et al. (2013). Caspian sea-level changes during the last millennium: Historical and geological evidence from the south Caspian Sea. *Climate of the Past*, *9*(4), 1645–1665. http://dx.doi.org/10.5194/cp-9-1645-2013
Nikurashin, M., & Ferrari, R. (2011). Global energy conversion rate from geostrophic flows into internal lee waves in the deep ocean. *Geophysical Research Letters*, *38*(8). https://doi.org/10.1029/2011GL046576
NOAA (1988). *Data Announcement 88-MGG-02 1988, Digital relief of the Surface of the Earth*. NOAA, National Geophysical Data Center.
Nycander, J. (2005). Generation of internal waves in the deep ocean by tides. *Journal of Geophysical Research*, *110*, (C10), https://doi.org/10.1029/2004jc002487
Pail, R., Bingham, R., Bingham, R., Braitenberg, C., Dobslaw, H., Eicker, A., et al. (2015). Science and user needs for observing global mass transport to understand global change and to benefit society. *Surveys in Geophysics*, *36*(6), 743–772. https://doi.org/10.1007/s10712-015-9348-9
Pedley, M., Paren, J. G., & Potter, J. R. (1986). The tidal spectrum underneath Antarctic ice shelves. *Journal of Geophysical Research*, *91*(C11), 13001. https://doi.org/10.1029/jc091ic11p13001
Pekeris, C. L. (1974). A derivation of Laplace's tidal equation from the theory of inertial oscillations. *Proceedings of the Royal Society of London*, *374*, 81–86. http://www.jstor.org/stable/2990346
Pérenne, N., & Pichon, A. (1999). Effect of barotropic tidal rectification on low-frequency circulation near the shelf break in the northern Bay of Biscay. *Journal of Geophysical Research: Oceans*, *104*, (C6), 13489–13506. https://doi.org/10.1029/1999jc900050
Piccioni, G., Dettmering, D., Bosch, W., & Seitz, F. (2019). TICON: TIdal CONstants based on GESLA sea-level records from globally located tide gauges. *Geoscience Data Journal*, *6*(2), 97–104. https://doi.org/10.1002/gdj3.72
Platzman, G. W. (1984). Planetary energy balance for tidal dissipation. *Reviews of Geophysics*, *22*(1), 73–84. https://doi.org/10.1029/rg022i001p00073
Ray, R. D. (1998). Ocean self-attraction and loading in numerical tidal models. *Marine Geodesy*, *21*(3), 181–192. https://doi.org/10.1080/01490419809388134
Ray, R. D. (1999). *A Global Ocean Tide Model From TOPEX/POSEIDON Altimetry: GOT99.2*. https://ntrs.nasa.gov/citations/19990089548
Ray, R. D. (2001). Resonant third-degree diurnal tides in the seas off Western Europe. *Journal of Physical Oceanography*, *31*(12), 3581–3586. https://doi.org/10.1175/1520-0485(2001)031⟨3581:RTDDTI⟩2.0.CO;2

Ray, R. D. (2013). Precise comparisons of bottom-pressure and altimetric ocean tides. *Journal of Geophysical Research: Oceans*, *118*(9), 4570–4584. https://doi.org/10.1002/jgrc.20336
Ray, R. D. (2017). On tidal inference in the diurnal band. *Journal of Atmospheric and Oceanic Technology*, *34*(2), 437–446. https://doi.org/10.1175/jtech-d-16-0142.1
Ray, R. D. (2020). First global observations of third-degree ocean tides. *Science Advances*, *6*(48), eabd4744. https://doi.org/10.1126/sciadv.abd4744
Ray, R. D., Loomis, B. D., Luthcke, S. B., & Rachlin, K. E. (2019). Tests of ocean-tide models by analysis of satellite-to-satellite range measurements: An update. *Geophysical Journal International*, *217*(2), 1174–1178. https://doi.org/10.1093/gji/ggz062
Ray, R. D., Luthcke, S. B., & Boy, J.-P. (2009). Qualitative comparisons of global ocean tide models by analysis of intersatellite ranging data. *Journal of Geophysical Research*, *114*, (C9), https://doi.org/10.1029/2009jc005362
Risbo, T. (1996). Fourier transform summation of Legendre series and D-functions. *Journal of Geodesy*, *70*(7), 383–396. https://doi.org/10.1007/s001900050028
Savcenko, R., & Bosch, W. (2010). *EOT11a—Empirical ocean tide model from multi-mission satellite altimetry* (Technical Report No. 89, p. 49). Deutsches Geodätisches Forschungsinstitut. hdl:10013/epic.43894.d001
Savcenko, R., Bosch, W., Dettmering, D., & Seitz, F. (2012). *EOT11a: Global Empirical Ocean Tide model from multi-mission satellite altimetry*. Deutsches Geodätisches Forschungsinstitut. https://doi.org/10.1594/PANGAEA.834232
Saynisch, J., Irrgang, C., & Thomas, M. (2018). Estimating ocean tide model uncertainties for electromagnetic inversion studies. *Annales Geophysicae*, *36*(4), 1009–1014. https://doi.org/10.5194/angeo-36-1009-2018
Schaeffer, N. (2013). Efficient spherical harmonic transforms aimed at pseudospectral numerical simulations. *Geochemistry, Geophysics, Geosystems*, *14*(3), 751–758. https://doi.org/10.1002/ggge.20071
Schaffer, J., Timmermann, R., Arndt, J. E., Kristensen, S. S., Mayer, C., Morlighem, M., & Steinhage, D. (2016). A global, high-resolution data set of ice sheet topography, cavity geometry, and ocean bathymetry. *Earth System Science Data*, *8*(2), 543–557. https://doi.org/10.5194/essd-8-543-2016
Schindelegger, M., Green, J. A. M., Wilmes, S.-B., & Haigh, I. D. (2018). Can We Model the Effect of Observed Sea Level Rise on Tides?. *Journal of Geophysical Research: Oceans*, *123*, (7), 4593–4609. https://doi.org/10.1029/2018jc013959
Schrama, E. J. O., & Ray, R. D. (1994). A preliminary tidal analysis of TOPEX/POSEIDON altimetry. *Journal of Geophysical Research*, *99*(C12), 24799. https://doi.org/10.1029/94jc01432
Scott, R. B., Goff, J. A., Naveira Garabato, A. C., & Nurser, A. J. G. (2011). Global rate and spectral characteristics of internal gravity wave generation by geostrophic flow over topography. *Journal of Geophysical Research*, *116*(C9). https://doi.org/10.1029/2011JC007005
Seiler, U. (1991). Periodic changes of the angular momentum budget due to the tides of the World Ocean. *Journal of Geophysical Research*, *96*(B6), 10287. https://doi.org/10.1029/91jb00219
Shum, C. K., Woodworth, P. L., Andersen, O. B., Egbert, G. D., Francis, O., King, C., et al. (1997). Accuracy assessment of recent ocean tide models. *Journal of Geophysical Research: Oceans*, *102*, (C11), 25173–25194. https://doi.org/10.1029/97jc00445
Spiridonov, E. A. (2018). Tidal Love numbers of degrees 2 and 3. *Izvestiya, Atmospheric and Oceanic Physics*, *54*(8), 911–931. https://doi.org/10.1134/S0001433818080133
St. Laurent, L., Alford, M., & Paluszkiewicz, T. (2012). An introduction to the special issue on internal waves. *Oceanography*, *25*(2), 15–19. https://doi.org/10.5670/oceanog.2012.37
Stammer, D., Ray, R. D., Andersen, O. B., Arbic, B. K., Bosch, W., Carrère, L., et al. (2014). Accuracy assessment of global barotropic ocean tide models. *Reviews of Geophysics*, *52*(3), 243–282. https://doi.org/10.1002/2014RG000450.Received
Sulzbach, R., Dobslaw, H., & Thomas, M. (2021). *Mass variations induced by ocean tide oscillations (TiME21) v. 1.0*. GFZ Data Services. https://doi.org/10.5880/GFZ.1.3.2021.001
Taguchi, E., Stammer, D., & Zahel, W. (2014). Inferring deep ocean tidal energy dissipation from the global high-resolution data-assimilative HAMTIDE model. *Journal of Geophysical Research: Oceans*, *119*(7), 4573–4592. https://doi.org/10.1002/2013JC009563
Tapley, B. D., Watkins, M. M., Flechtner, F., Reigber, C., Bettadpur, S., Rodell, M., et al. (2019). Contributions of GRACE to understanding climate change. *Nature Climate Change*, *9*(5), 358–369. https://doi.org/10.1038/s41558-019-0456-2
Thomas, M., & Sündermann, J. (1999). Tides and tidal torques of the world ocean since the last glacial maximum. *Journal of Geophysical Research: Oceans*, *104*, (C2), 3159–3183. https://doi.org/10.1029/1998jc900097
Thomas, M., Sündermann, J., & Maier-Reimer, E. (2001). Consideration of ocean tides in an OGCM and impacts on subseasonal to decadal polar motion excitation. *Geophysical Research Letters*, *28*(12), 2457–2460. https://doi.org/10.1029/2000GL012234
Velay-Vitow, J. G., Peltier, W. R., & Stuhne, G. R. (2020). Out of the Ice Age: Megatides of the Arctic Ocean and the Bølling-Ållerød, Younger Dryas Transition. *Geophysical Research Letters*, *47*, (23), https://doi.org/10.1029/2020gl089870
Wahr, J. M. (1981). Body tides on an elliptical, rotating, elastic and oceanless earth. *Geophysical Journal of the Royal Astronomical Society*, *64*(3), 677–703. https://doi.org/10.1111/j.1365-246x.1981.tb02690.x
Wahr, J. M., & Sasao, T. (1981). A diurnal resonance in the ocean tide and in the Earth's load response due to the resonant free 'core nutation'. *Geophysical Journal of the Royal Astronomical Society*, *64*, (3), 747–765. https://doi.org/10.1111/j.1365-246x.1981.tb02693.x
Wang, H., Xiang, L., Jia, L., Jiang, L., Wang, Z., Hu, B., & Gao, P. (2012). Load Love numbers and Green's functions for elastic Earth models PREM, iasp91, ak135, and modified models with refined crustal structure from Crust 2.0. *Computers & Geosciences*, *49*, 190–199. https://doi.org/10.1016/j.cageo.2012.06.022
Warschalowitsch, D. A., Varshalovich, D., & Moskalev, A. N. (1988). *Quantum theory of angular momentum*. World Scientific Pub.
Weis, P., Thomas, M., & Sündermann, J. (2008). Broad frequency tidal dynamics simulated by a high-resolution global ocean tide model forced by ephemerides. *Journal of Geophysical Research*, *113*, (C10), http://dx.doi.org/10.1029/2007jc004556
Wiese, D. N., Killett, B., Watkins, M. M., & Yuan, D. N. (2016). Antarctic tides from GRACE satellite accelerations. *Journal of Geophysical Research: Oceans*, *121*(5), 2874–2886. https://doi.org/10.1002/2015JC011488
Wilmes, S.-B., Green, J. A. M. (2014). The evolution of tides and tidal dissipation over the past 21,000 years. *Journal of Geophysical Research: Oceans*, *119*, (7), 4083–4100. https://doi.org/10.1002/2013jc009605
Wunsch, C. (1975). Internal tides in the ocean. *Reviews of Geophysics*, *13*, (1), 167. https://doi.org/10.1029/rg013i001p00167
Zahel, W. (1977). A global hydrodynamic-numerical 1°-model of the ocean-tides; the oscillation system of the M2-tide and its distribution of energy dissipation. *Annales Geophysicae*, *33*, 31–40.
Zahel, W. (1978). The influence of solid Earth deformations on semidiurnal and diurnal oceanic tides. In *Tidal friction Earth's rotation* (pp. 98–124). Springer Verlag. https://doi.org/10.1007/978-3-662-40203-0_9
Zahel, W., & Müller, M. (2005). The computation of the free barotropic oscillations of a global ocean model including friction and loading effects. *Ocean Dynamics*, *55*(2), 137–161. https://doi.org/10.1007/s10236-005-0029-y

Zhao, Z., Alford, M. H., Girton, J. B., Rainville, L., & Simmons, H. L. (2016). Global observations of open-ocean mode-1 M_2 internal tides. *Journal of Physical Oceanography*, *46*(6), 1657–1684. https://doi.org/10.1175/JPO-D-15-0105.1

Zhao, Z., Alford, M. H., Girton, J., Johnston, T. M. S., & Carter, G. (2011). Internal tides around the Hawaiian Ridge estimated from multi-satellite altimetry. *Journal of Geophysical Research*, *116*, (C12), https://doi.org/10.1029/2011jc007045

Zweng, M. M., Reagan, J. R., Seidov, D., Boyer, T. P., Antonov, J. I., Locarnini, R. A., et al. (2018). *World Ocean Atlas 2018, Volume 2: Salinity*. World Ocean Atlas 2018 (Vol. 2, p. 50). Retrieved from https://www.ncei.noaa.gov/sites/default/files/2020-04/woa18_vol2.pdf